PTZ Camera Tampering Correction Using IMUs

Ludvig Hansson
Måns Lindeberg

LUND UNIVERSITY
Department of Automatic Control

MSc Thesis
TFRT-6161
ISSN 0280-5316

Department of Automatic Control
Lund University
Box 118
SE-221 00 LUND
Sweden

Printed in Sweden by Tryckeriet i E-huset
Lund 2022

Abstract

The Pan-Tilt-Zoom (PTZ) camera is a type of camera that covers large areas, up to 360°, in addition to zoom. Some of these cameras are susceptible to tampering, which means that an additional angle measurement feedback is necessary to detect such attempts. This thesis has evaluated the possibility of using MEMS-based IMUs to solve this problem. An advantage of such a system over other solutions, such as optical and magnetic encoders, is the decreased cost and complexity. The difficulty of using IMUs is that they are susceptible to drift in horizontal rotations in pan and require advanced signal processing to be reliable in demanding environments. Results showed that it was possible to correct tampering by using two IMUs, one on the fixed part of the camera and one on the moving part of the camera. It was then possible to track and correct tampering attempts with an average error of 1.0° in pan and 0.7° in tilt. The solution works when the camera is mounted on both fixed and moving objects. Notably, the solution proved to be much cheaper than alternative methods. Additionally, it proved to be robust against vibrations and shocks and within the performance requirements of the tested model.

Additional methods were suggested for the system to track absolute orientation, for example, to be able to move the camera to pre-set positions. However, further work is needed to increase robustness in applications where the camera is mounted on objects that can rotate in roll or pitch.

Acknowledgments

We would like to thank our supervisor Anton Cervin and examiner Kristian Soltesz at the Department of Automatic Control at LTH for the help and feedback during our work. We also want to thank Anders Robertsson for the valuable help in understanding dynamical navigations.

Lastly, we want to extend a big thank you to the PTZ Electronic Team at Axis Communications, and especially our supervisor Marcus Romner, for the support and help we have received during our work.

Contents

1. Introduction **11**
1.1 Background 11
1.2 Problem Formulation 12
1.3 Scope & Delimitation 13

2. Theory **15**
2.1 Stepper Motor & Positioning Feedback 15
2.1.1 Encoder Feedback 16
2.1.2 IMU Feedback 16
2.2 Orientation and Rotations 17
2.2.1 Reference Frames 17
2.2.2 Coordinate Systems 17
2.2.3 Rotations 19
2.2.3.1 Rotation Matrices 19
2.2.3.2 Quaternions 20
2.3 Heading Estimation 22
2.3.1 Direct Tait-Bryan Angle Method 22
2.3.2 Complementary Filter 23
2.3.3 Factored Quaternion Algorithm 23
2.3.4 Mahony Filter 26
2.3.5 Madgwick Filter 27
2.3.6 Summary of methods for attitude estimation 29
2.4 Signal processing 30
2.4.1 Sampling data 30
2.4.2 Low-Pass Filters 31
2.4.2.1 Simple Moving Average 31
2.4.2.2 Exponential Weighted Moving Average 31
2.4.3 Gyroscope Bias Compensation 31
2.4.4 Magnetometer Calibration 32

3. Experimental Setup **35**
3.1 Material 35

3.1.1 PTZ Camera . . . 35
3.1.2 STMicroelectronics Nucleo-G070RB . . . 37
3.1.3 InvenSense ICM20948 MEMS IMU . . . 37
3.1.3.1 3-Axis Accelerometer . . . 37
3.1.3.2 3-Axis Gyroscope . . . 37
3.1.3.3 3-Axis Magnetometer . . . 37
3.2 InvenSense ICM20602 MEMS IMU . . . 37
3.3 Cost of IMUs . . . 38
3.4 Test Environment . . . 38
4. IMU Measurements **41**
4.1 Gyroscope Bias . . . 41
4.2 Acceleration Noise . . . 43
4.3 Magnetometer Disturbances . . . 43
5. Testing & Evaluation **47**
5.1 Fixed Axis . . . 47
5.1.1 Pan Result . . . 47
5.1.2 Tilt Result . . . 49
5.2 Sensor Fusion Algorithm . . . 50
5.2.1 Continuous Measurements . . . 51
5.2.2 Sweep Measurements . . . 52
5.2.3 Error Interpolation . . . 54
5.3 Tampering Measurements . . . 55
5.3.1 Pan Measurements . . . 56
5.3.2 Tilt Measurements . . . 58
5.4 Vibration Measurements . . . 61
5.5 Conclusion . . . 63
6. Final System **67**
6.1 Design . . . 68
6.1.1 Motion Triggered Differential Madgwick . . . 68
6.1.2 Double IMU sensors . . . 69
6.1.3 Motion State Sampling . . . 70
6.1.4 Interpolation Error Compensation . . . 71
6.2 Sensor Calibration . . . 72
6.2.1 Software Design . . . 72
6.2.2 Parameters . . . 74
6.3 Economy . . . 74
6.4 Performance results . . . 75
6.4.1 Mounted on non-moving object . . . 75
6.4.2 Mounted on moving object . . . 76
6.4.3 Vibration Tolerance . . . 76
7. Discussion **79**
7.1 Solutions for Tampering Detection Comparison . . . 79

7.2 Limitations of Final System 80
7.3 Further work 81
8. Conclusion **82**
Bibliography **83**
8.1 Error Interpolation Polynomial 87

List of Abbreviations

CF Complementary Filter

DLPF Digital Low Pass Filter

DOF Degree of Freedom

EKF Extended Kalman Filter

EMA Exponential Moving Average

FSR Full-scale Range

FQR Factored Quaternion Algorithm

IIR Infinite Impulse Response

IMU Inertial Measurement Unit

KF Kalman Filter

LOC Lines of Code

MEMS Micro-Electromechanical System

MSS Motion State Sampling

MTDM Motion Triggered Differential Madgwick

NMNI No Motion-No Integartion

PTZ Pan-Tilt-Zoom

SFA Sensor Fusion Algorithm

SMA Simple Moving Average

1

Introduction

This chapter provides a background which highlights important facts about PTZ cameras and history of the IMU. Furthermore, *Section* 1.2 consists of a problem formulation that explains the aim of this thesis. Finally, *Section* 1.3 discusses scope and limitations which helps narrow down the problem formulation.

1.1 Background

It is increasing in popularity to use cameras for surveillance in public areas where people want to feel safe or in private areas where someone has something to monitor. There is a wide variety of different types. For example, the Pan-Tilt-Zoom (PTZ) cameras can cover large areas, up to 360°, combined with optical and digital zoom. A PTZ camera differs from fixed-position cameras by requiring more complex mechanics, for example, electric motors and belts. However, the added degrees of freedom (DOF) also allow for easier camera tampering. External influences can make the camera lose its position if positioned in an exposed environment. Someone can easily change the camera's field of view, which means there is a need for feedback to validate that the current position has not been tampered with. The list of possible feedback solutions are long. However, one that has grown popular is the micro-electromechanical-system (MEMS) based IMU because of its reasonable trade-off in price and precision. The IMU's main components are gyroscope and accelerometer, and sometimes also a magnetometer. The IMUs were developed during the 20th century with a primary goal to be used in the military industry. Since then, they have been integrated in numerous other products such as smartphones, cars and wearables, to name a few.

A prominent company in the market of surveillance cameras is Axis Communications AB (Axis). The company is continuously developing several different models, and one of their popular segments is the PTZ camera. This master thesis is conducted at Axis PTZ department with the main goal to investigate if it is possible to get a reliable heading feedback using MEMS-based IMUs.

1.2 Problem Formulation

Axis currently has two options for feedback to their PTZ cameras: optical and magnetic. The magnetic feedback solution is more expensive but has an advantage in resolution over the optical, see *Table* 1.1 for comparison. The feedback is a costly part of the electronics budget, hence a cheap solution with good resolution is to prefer.

Table 1.1 Resolution for the two existing feedback solutions

Magnetic feedback	$\pm 0.005°$
Optical feedback	$\pm 9°$

As mentioned in *Section* 1.1, MEMS-based IMUs have become a cheap option for pose estimation. The purpose of this thesis will be, on behalf of Axis, to investigate the pose estimation performance of MEMS-based IMUs compared to the magnetic and optical feedback solution.

This study is divided into three investigations. The first two involves placing an IMU in two different positions on the moving part on a PTZ camera. The last sub problem involves placing another IMU in a non-moving part on the same camera.

- One IMU is placed in the horizontal rotation axis on the moving part of the camera, and one is placed on the vertical axis on the moving part.
- One IMU is placed on a part of a camera which can rotate in both pan and tilt.
- One IMU is placed on a part of a camera which can not rotate in pan or tilt, and one that can rotate in pan and tilt.

Another goal is to detect if tampering has occurred. Since the camera can be mounted on both moving and non-moving objects, there are four different cases that have to be handled to get as general a solution as possible:

1. When the camera is mounted on a non-moving object:
   a) Camera is tampered while not moving.
   b) Camera is tampered while moving.
2. When the camera is mounted on a moving object:
   a) Camera is tampered while not moving.
   b) Camera is tampered while moving.

1.3 Scope & Delimitation

The study has focused on getting an accurate and robust pose estimation from one or several IMUs. It can be divided into three main parts:

1. Pre-study on:
    a) Feedback solutions for pose estimation
    b) Signal processing techniques
    c) Transformation of coordinate systems
    d) IMU's strengths and weaknesses
2. Microcontroller programming and implementation of IMU and control algorithms.
3. Testing:
    a) IMU drift and noise compensation
    b) IMU heading estimation
    c) IMU tampering detection and vibration sensitivity
4. Evaluation of final system with the goal of getting as accurate and robust orientation estimate as possible with the magnetic feedback solution as reference, see *Table* 1.1.

2

Theory

This chapter will present the underlying theory, which is the foundation for this report and necessary to grasp the content in the subsequent chapters. The chapter has been divided into *Section* 2.1 that presents different types of feedback solutions, *Section* 2.2 that presents reference frames, orientation estimation techniques and rotations. *Section* 2.3 discusses attitude and heading estimation and lastly *Section* 2.4 presents signal processing techniques that are used throughout the report.

2.1 Stepper Motor & Positioning Feedback

A stepping motor is a type of Brushless DC Motor (BLDC) that, ideally, does not need closed-loop sensor feedback to control its position since it moves in discrete steps. This property is typically appropriate in applications requiring precise automated positioning, such as robotics or camera positioning. An alternative to a stepping motor is to use a closed-loop servo motor that requires external positioning feedback to track the rotor position, which in turn provides higher accuracy. The upside of stepping motors is that they are cheaper and more straightforward than a servo motor since they do not require feedback circuitry. However, the downside is that it loses its positioning (relative step position to some initialized state) if it is over-torqued. At the same time, a servo motor would detect such a difference between the desired position and the actual position. Therefore, stepping motors are generally not used in systems where the system is exposed to external load during acceleration, such as if an external force counteracts the supposed rotation. It is more commonly used in applications operating with static load and low acceleration [Jones, 2001]. When using stepping motors, it is common to use a hold current when the motors are idle to prevent them from losing position. However if the motors are used in an application where such an external force could make them lose position, adding an external feedback input to a stepping motor controller makes it possible to achieve tampering detection and error correction while having a more cost-effective solution than servomotors.

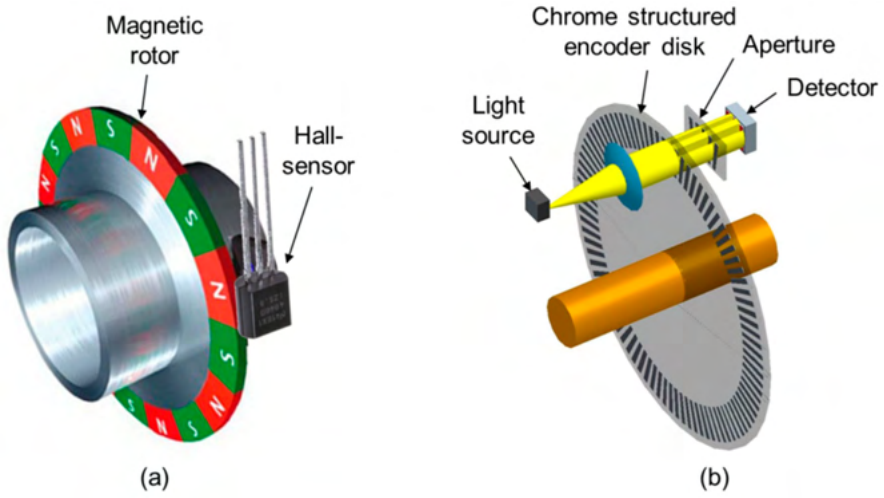

Figure 2.1 Operating principle of (a) magnetic encoder and (b) optical encoder. [Seybold et al., 2019, Fig 1]

2.1.1 Encoder Feedback

Today, many different techniques are used for rotational positioning feedback to stepping motors. One method is to use encoders for precise control, typically capacitive, optical, or magnetic encoders. Optical encoders are the most common and consist of a LED, two photosensors in quadrature, and a disk in between with engraved splits, creating different light patterns depending on the position. The sensors pick up the pattern and can thereby determine position. The resolution then depends on the engraved splits in the disk. An advantage of optical encoders is that they offer high resolution, but a drawback is that it is sensible to dirt and dust [Schweber, 2021]. It is better to use magnetic encoders in such environments. This type of encoder decode the rotational position from a hall-sensor measuring magnetic flux of permanent magnets since these are more reliable in dusty and humid environments. The achievable resolution then depends on the number of sensors and the number of pole pairs on the rotating magnet [Seybold et al., 2019]. See Figure 2.1 for a comparison between optical and magnetic encoders.

2.1.2 IMU Feedback

An alternative method is to use an inertial measurement unit (IMU), typically in a 6-axis or 9-axis version. A 6-axis IMU includes an accelerometer that measures acceleration in a local 3-axis Cartesian coordinate system and a gyroscope that measures angular velocity in Tait-Bryan angles in the same local coordinate system as the accelerometer, see *Figure* 2.4 for illustration. However, a 9-axis IMU also incorporates a magnetometer that measures the cartesian coordinates' magnetic field.

The magnetometer component is valuable when the application needs to know the object's orientation relative to the earth's magnetic field. IMUs are generally less expensive than encoders but are not as accurate. They are sensitive to noise and bias error which accumulates when integrating gyroscope data, which in turn cause the pose estimation to "drift" with time. Therefore, IMUs require considerably more signal processing before being considered reliable.

2.2 Orientation and Rotations

Before diving into the many ways of calculating orientations using an IMU, it is important to explain the different coordinate systems and frames that the following sections will mention. For example, a magnetometer measures magnetic field strength in linear cartesian coordinates in the earth frame, whereas the gyroscope measures the angular velocity in Tait-Bryan coordinates in the inertial frame.

2.2.1 Reference Frames

In order to estimate the orientation of the IMU, it is important to account for the relativity of coordination frames that it moves within. Essentially there are four frames that must be taken into consideration: *the body frame, the natural frame, the earth frame* and the *inertial frame*, see *Figure* 2.2. The inertial frame is the static frame with its center in the core of the earth. The earth frame is the frame that has its center at the earth's core but also follows the rotation of the earth relative to the inertial frame. Note that the IMU measures the angular velocity and acceleration in the inertial frame, which means that it also measures the angular rotation of the earth as well as the rotational speed of the earth and the *Coriolis acceleration*. The natural frame is the local geographical frame that the position of the IMU is relative to. [Kok et al., 2017].

2.2.2 Coordinate Systems

The Cartesian coordinate system represents numerical coordinates along perpendicular linear axes. An accelerometer measures acceleration in this coordinate system, while a magnetometer measures magnetic field strength linearly as well. *Figure* 2.3 shows the linear x, y & z axes that is referred to throughout the report. Note that the z-axis points downwards because it is following the direction of the force of gravity.

The Cartesian coordinate system is not ideal for rotations which is why Peter Guthrie Tait and George H. Bryan developed the Tait-Bryan coordinate system, principally to more easily represent rotations meant for aerospace engineers. Tait-Bryan coordinates measures orientation in 3D space using *yaw* (ψ), *pitch* (φ), and *roll* (θ). The definition can be expressed geometrically by the angle difference between the earth frame and the body Frame. Referring back to *Figure* 2.2, ψ is the angle between z_e and z_n, φ is the angle between y_e and y_n, and θ is the angle be-

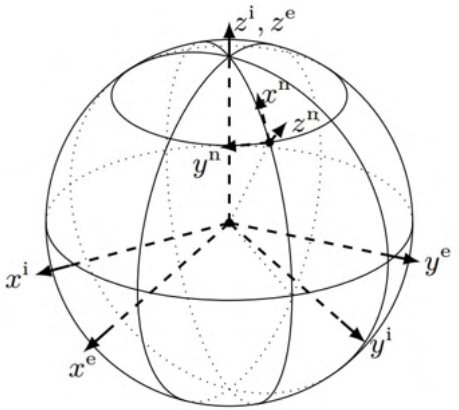

Figure 2.2 Frames of reference - body frame, natural frame, earth frame and inertial frame. The exponent in the axis name indicates which frame it is [Kok et al., 2017, Fig 2.1].

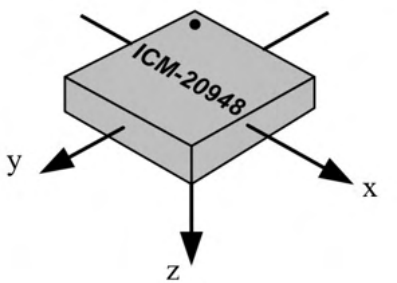

Figure 2.3 Cartesian coordinate system [InvenSense, 2021, Fig 13]

tween x_e and x_n. This coordinate system can therefore be used to represent rotations around the linear x, y and z axes [Allgeuer and Behnke, 2018]. *Figure* 2.4 shows the yaw, pitch and roll that are used throughout the report.

When using Tait-Bryan angles, there is a possibility that *gimbal lock* will occur. The phenomenon leads to losing one or more degrees of freedom in the heading estimation, making it corrupt. The consequence is that it becomes unattainable to describe the orientation uniquely. When one of the angles yaw, pitch or roll, see *Figure* 2.4, is near $\pm 90°$, two planes will have the same orientation, and after their alignment, there is a possibility that the planes will lock and hence one degree of

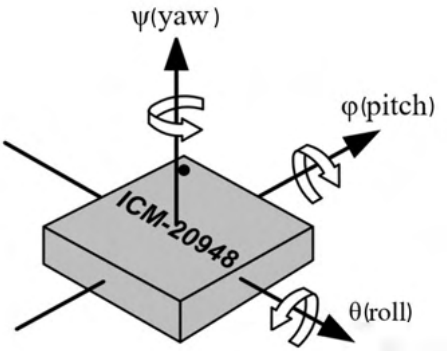

Figure 2.4 Tait-Bryan angles [InvenSense, 2021, Fig 12]

freedom is lost [Mansur et al., 2020].

2.2.3 Rotations

2.2.3.1 Rotation Matrices A rotation matrix is used to rotate points or vectors in space. This kind of transformation is often used to calculate a point's position or vector's direction in another coordinate system than the currently used. When having a three-dimensional space, three basic rotations are needed, one for each axis. These basic rotations are then multiplied to get a rotation matrix for the whole space [Freidovich, 2017]. The roll rotation (around x-axis) can be formulated as

$$R_x(\theta) = \begin{pmatrix} 1 & 0 & 0 \\ 0 & \cos\theta & -\sin\theta \\ 0 & \sin\theta & \cos\theta \end{pmatrix}. \tag{2.1}$$

For pitch rotation (around the y-axis) the matrix becomes

$$R_y(\varphi) = \begin{pmatrix} \cos\varphi & 0 & \sin\varphi \\ 0 & 1 & 0 \\ -\sin\varphi & 0 & \cos\varphi \end{pmatrix}. \tag{2.2}$$

The final rotation, in yaw (around z-axis), is

$$R_z(\psi) = \begin{pmatrix} \cos\psi & -\sin\psi & 0 \\ \sin\psi & \cos\psi & 0 \\ 0 & 0 & 1 \end{pmatrix}. \tag{2.3}$$

The resulting rotation matrix comes from multiplying the basic rotations mentioned above. The order of rotations matter, following a left-to-right rule. For example if having the order roll-pitch-yaw in a rotation, then the transformation matrix becomes

$$R = R_z(\psi)R_y(\varphi)R_x(\theta) = \begin{pmatrix} \cos\psi\cos\varphi & \cos\psi\sin\varphi\sin\theta - \sin\psi\cos\theta & \cos\psi\sin\varphi\cos\theta + \sin\psi\sin\theta \\ \sin\psi\cos\varphi & \sin\psi\sin\varphi\sin\theta + \cos\psi\cos\theta & \sin\psi\sin\varphi\cos\theta - \cos\psi\sin\theta \\ -\sin\varphi & \cos\varphi\sin\theta & \cos\varphi\cos\theta \end{pmatrix} \tag{2.4}$$

.

If having another order in rotations then the matrix multiplication comes in another order, resulting in a different rotation matrix.

2.2.3.2 Quaternions The quaternion system was brought in 1843 by *W.R Hamilton*, by the realisation that a fourth dimension could be used to simplify 3 dimensional multiplications. It uses three complex dimensions $\boldsymbol{i}$, $\boldsymbol{j}$, and $\boldsymbol{k}$ where

$$\boldsymbol{i}^2 = \boldsymbol{j}^2 = \boldsymbol{k}^2 = \boldsymbol{ijk} = -1, \tag{2.5}$$

and one real such that the quaternion q becomes

$$q = q_0 + \boldsymbol{q} = q_0 + q_1\boldsymbol{i} + q_2\boldsymbol{j} + q_3\boldsymbol{k}. \tag{2.6}$$

The set of quaternions together with multiplication and addition forms a non-commutative ring, such that the multiplication operation $A \times B \neq B \times A$. More precisely, addition of two quaternions q_A and q_B are defined as:

$$q_A + q_B = (q_{A,0} + q_{B,0}) + (q_{A,1} + q_{B,1})\boldsymbol{i} + (q_{A,2} + q_{B,2})\boldsymbol{j} + (q_{A,3} + q_{B,3})\boldsymbol{k}. \tag{2.7}$$

Based on the definition in *Equation* 2.5 it is straightforward to derive and simplify the product of two quaternions vectors as:

$$q_A q_B = q_{A,0}q_{B,0} - \boldsymbol{q_A} \cdot \boldsymbol{q_B} + q_{A,0}\boldsymbol{q_A} + q_{B,0}\boldsymbol{q_B} + \boldsymbol{q_A} \times \boldsymbol{q_B} \tag{2.8}$$

Note that the product of two quaternions again becomes a quaternion.

Furhtermore, the *complex conjugate*, q^* of a quaternion is defined as:

$$q^* = q_0 - \boldsymbol{q} = q_0 - q_1\boldsymbol{i} - q_2\boldsymbol{j} - q_3\boldsymbol{k}. \tag{2.9}$$

Such that

$$qq^* = 2q_0. \tag{2.10}$$

Lastly, the inverse of a quaternion becomes

$$q^{-1} = \frac{q^*}{|q|^2} \tag{2.11}$$

where the norm is defined as

$$|q| = \sqrt{qq^*}. \tag{2.12}$$

A quaternion with a norm of 1 is called a *unit quaternion* and the reason why they are of special importance is that they make it possible to use the quaternion in $\mathbb{R}^4$ to rotate a $\mathbb{R}^3$ vector. A rotation with an angle of θ on a vector $v \in \mathbb{R}^3$, represented in quaternion space as $p = (0, \boldsymbol{v})$, can be done forming an unit quaternion:

$$q = q_0 + \boldsymbol{q} = \cos\frac{\theta}{2} + \boldsymbol{u}\sin\frac{\theta}{2}, \tag{2.13}$$

$\boldsymbol{u} = \frac{\boldsymbol{q}}{||\boldsymbol{q}||}$ and rotate the coordinate frame of v to its new orientation p' with the operation

$$p' = qpq^{-1}. \tag{2.14}$$

In addition to the effectiveness, the advantage of quaternion rotations over rotation matrices in Tait-Bryan coordinates, is that these are not susceptible to gimbal lock. The proof of this is left out but can be found in [Kuipers, 2020].

It is important to mention that even if the rotations are performed in quaternion space, it is still possible to translate it back into Tait-Bryan angles yaw, pitch and roll:

$$\begin{bmatrix} \varphi \\ \theta \\ \psi \end{bmatrix} = \begin{bmatrix} atan2(q_0q_1 + q_2q_3, 1 - 2(q_2^2 + q_2^2)) \\ asin(2(q_0q_2 - q_3q_1)) \\ atan2(2(q_0q_3 + q_1q_2), 1 - 2(q_2^2 + q_3^2)) \end{bmatrix}. \tag{2.15}$$

2.3 Heading Estimation

Pose estimations give the orientation of the body frame in the "natural" or "reference" frame. A gyroscope measures the angular velocity in Tait-Bryan angles, see *Figure* 2.4, whereas the accelerometer and magnetometer measures the acceleration and magnetic field strength in linear coordinates, see *Figure* 2.3. About some initial state, the heading of an object with an IMU can be estimated by individually or in combination *a)* integrating the angular velocity in order to determine the angle in yaw, pitch, and roll, *b)* determine the pitch and roll by observing the accelerometer values in relation to the force of gravitational vector *c)* determine the yaw by double integrating accelerometer data in x & y plane knowing the radius of the rotation and *d)* determine the yaw by measuring the magnetic field strength of the earth [Yang et al., 2017].

As discussed in Section 2.1.2 the accelerometer is susceptible to noise and the gyroscope to bias. The gyroscope is also susceptible to noise but far less than the accelerometer. In other words, the gyroscope provides accurate measurements in the short term and the accelerometer in the long term. The time frame depends on how much the gyroscope drifts, but even the most advanced gyroscopes have an error that increases with time. It is therefore desirable to combine the signals using *Sensor Fusion Algorithm* (SFA), such as a *Kalman Filter* (KF), an *Extended Kalman Filter* (EKF), or *Complementary Filter* (CF) to get the best of both worlds. Using SFA, the combination of gyroscope *a)* and accelerometer *b)* and/or the magnetometer *d)* [Fan et al., 2017]. A downside with magnetometers is that they are sensitive to magnetic disturbances caused by Electromagnetic Interference (EMI) from power cords, motors, and ferromagnetic objects, that are difficult to filter out. Nonetheless, researchers have suggested several methods that compensate for dynamic magnetic disturbance, for example, by applying a nonlinear optimization approach using Kalman Filters. [Wu, 2019]

2.3.1 Direct Tait-Bryan Angle Method

The most common heading estimation algorithm using an IMU is to calculate the Tait-Bryan angles pitch directly from trigonometric operations on the accelerometer and magnetometer and numerically integrate the angular velocity from the gyroscope. It is called the *Direct Tait-Bryan Angle Method*. [Pedley, 2013]

From the linear accelerometer readings $\boldsymbol{a} = [a_x, a_y, a_z]$, the pitch φ, is calculated directly with

$$\varphi = atan2(a_y, a_z). \tag{2.16}$$

The roll can be determined similarly with

$$\theta = -atan2(a_x, \sqrt{a_x^2 + a_z^2}). \tag{2.17}$$

In both cases, it is assumed the rotation sequence is x-y-z.

Furthermore, the gyroscope can be numerically integrated in order to obtain all three angles. Remember that the integration leads to drift. Additionally, since the roll and pitch are already calculated using the accelerometer, the yaw angle is simply determined given the angular velocity $\boldsymbol{\omega} = [\omega_x, \omega_y, \omega_z]$ with

$$\psi_{gyro} = \int \omega_z dt. \tag{2.18}$$

Additionally, since the gyroscope is calculated in the body frame, it needs to be rotated in to the reference frame. The most straightforward way is to construct a rotation matrix given the roll and pitch angles in *Equation* 2.16 and 2.17.

Using a 9-axis IMU, it is also possible to retrieve the absolute yaw angle given the magnetic field strength, $\boldsymbol{m} = [m_x, m_y, m_z]$, from the magnetometer, again by incorporating the already retrieved pitch, φ, and roll , θ, angles from the accelerometer to rotate it into the reference frame:

$$\psi_{mag} = atan2(-m_y \cos\varphi + m_z \sin\varphi, m_x \cos\theta + m_y \sin\varphi \sin\theta + m_z \cos\varphi \sin\theta). \tag{2.19}$$

2.3.2 Complementary Filter

A second popular heading estimation algorithm is the Complementary Filter (CF). The different characteristics of accelerometer, gyro, and magnetometer means that they can contribute with diverse information. As discussed in *Chapter* 2.3 the gyro provides reliable short-term measurements, the accelerometer long-term measurements, whereas the magnetometer is sensible to magnetically unstable environments. Therefore, it is desirable to fuse the sensor data using an SFA to increase the accuracy of the resulting pose estimation. The most common ones are Kalman-based filters and Complementary Filter. The complementary filter has been praised for its simplicity while still providing good performance. In contrast, Kalman-based filters tend to be more difficult to implement and require more computational power.

A downside with the complementary filter is that additional measures are needed to rotate the gyroscope measurements into the reference frame to get the correct yaw result over the full pitch range. It is achieved using either quaternions or rotation matrices. [Mahmood et al., 2016]

2.3.3 Factored Quaternion Algorithm

A third prevalent method is the *Factored Quaternion Algorithm* (FQA) which circumvents the singularity problem in Direct Tait-Bryan Angle Method by performing the rotations in quaternion space.

Assuming that the accelerometer initial state is facing downwards along with the force of gravity such that $a_{init} = [0, 0, g]$. A pitch angle, θ, from this initial state will directly lead to the accelerometer readings $a_x = g \sin\theta$ and $a_z = -g \cos\theta$. Combining with the resulting unit quaternion equation in *Equation* 2.13, the unit rotation quaternion in pitch becomes

$$q_p = \cos\frac{\theta}{2}(1\ 0\ 0\ 0) + \sin\frac{\theta}{2}(0\ 0\ 1\ 0). \tag{2.20}$$

Proceeding with the unit rotation quaternion for roll angle, changing the roll results in that $a_y = -g \cos\theta \sin\varphi$ and $a_z = -g \cos\theta \cos\varphi$, from which the roll rotation unit quaternion could be calculated as

$$q_r = \cos\frac{\varphi}{2}(1\ 0\ 0\ 0) + \sin\frac{\varphi}{2}(0\ 1\ 0\ 0). \tag{2.21}$$

Since the accelerometer is unable to determine yaw, either the gyroscope or the magnetometer data must be used. As discussed above, one way to achieve the yaw quaternion is to first solve for pitch, q_p and roll, q_r and then rotate it together with the normalized accelerometer vector into the earth frame (*note that the accelerometer measures in inertial frame and magnetometer in earth frame*). Outgoing from the magnetometer readings in the body frame

$$m^b = \begin{bmatrix} m_x \\ m_y \\ m_z \end{bmatrix}, \tag{2.22}$$

the yaw measurements are rotated into the earth frame with the operation presented in *Equation* 2.5, such that the magnetometer reading, m^e, becomes

$$m^e = q_p q_r m^b q_r^{-1} q_p^{-1}. \tag{2.23}$$

However, the rotated xy-plane may not align with the local normalized geomagnetic field, or sometimes called the "true north". except for the yaw angle, ψ, such that

$$\begin{bmatrix} n_x \\ n_y \end{bmatrix} = \begin{bmatrix} \cos\psi & -\sin\psi \\ \sin\psi & \cos\psi \end{bmatrix} \begin{bmatrix} m_x^e \\ m_y^e \end{bmatrix}. \tag{2.24}$$

Because IMU magnetometers are susceptible to interference which causes the vectors to differ in length, it is desirable to normalize the magnetic x-y plane, M, in the earth frame;

$$M = \begin{bmatrix} M_x \\ M_y \end{bmatrix} = \frac{1}{\sqrt{m_x^{e\,2} + m_y^{e\,2}}} \begin{bmatrix} m_x^e \\ m_y^e \end{bmatrix}, \tag{2.25}$$

and the x-y plane of the known local geomagnetic field, N, such that;

$$N = \begin{bmatrix} N_x \\ N_y \end{bmatrix} = \frac{1}{\sqrt{n_x^2 + n_y^2}} \begin{bmatrix} n_x \\ n_y \end{bmatrix}. \tag{2.26}$$

In turn solving for $\cos\psi$ and $\sin\psi$ results in

$$\begin{bmatrix} \cos\psi \\ \sin\psi \end{bmatrix} = \begin{bmatrix} M_x & M_y \\ -M_y & M_x \end{bmatrix} \begin{bmatrix} N_x \\ N_y \end{bmatrix} \tag{2.27}$$

from which ψ is extracted and thereafter put into forming the yaw unit rotation quaternion;

$$q_y = \cos\frac{\psi}{2}(1\ 0\ 0\ 0) + \sin\frac{\psi}{2}(0\ 0\ 0\ 1). \tag{2.28}$$

The orientation, $\hat{\boldsymbol{q}}$, is then fully described by the quaternion;

$$\hat{\boldsymbol{q}} = \boldsymbol{q_y q_p q_r}. \tag{2.29}$$

To use the gyroscope in quaternion space, it is first necessary to form the the angular rate, $\boldsymbol{\omega} \in \mathbb{R}^4$, such that

$$\bar{\omega} = \begin{bmatrix} 0 & \omega_x & \omega_y & \omega_z \end{bmatrix}. \tag{2.30}$$

The angular rate, $\boldsymbol{\omega}$, which describes the rate of change, is numerically integrated using the *Runge-Kutta* method with the initial value problem

$$\frac{d\hat{\boldsymbol{q}}_{\boldsymbol{t}}}{dt} = \frac{1}{2} \cdot \hat{\boldsymbol{q}}_{\boldsymbol{t}} \bar{\boldsymbol{\omega}} \tag{2.31}$$

where, $\hat{\boldsymbol{q}}_{\mathbf{o}} = [1,0,0,0]$. The resulting orientation is then described by the integrated quaternion at time t as

$$\hat{\boldsymbol{q}}_{\boldsymbol{t}} = \hat{\boldsymbol{q}}_{\boldsymbol{t-1}} + \frac{\Delta t}{2} \otimes \hat{\boldsymbol{q}}_{\boldsymbol{t-1}}. \tag{2.32}$$

where Δt denotes the sample time.

If both the magnetometer and the gyroscope were to be used in determining yaw, an additional SFA, such as the Complementary Filter, is needed.

A positive aspect of the FQA algorithm is that pitch and roll are decoupled from the magnetometer and thus unaffected by magnetic disturbances. Additionally, rotations are easily performed since they are performed in quaternion space [Yi et al., 2018].

2.3.4 Mahony Filter

A fourth popular sensor fusion algorithm is the quaternion-based PI-regulator approach known as the *Mahony Filter*. It is based on a complementary filter that provides reference frame rotation and bias correction to obtain accurate yaw estimation results over the entire tilt range. A high-level overview flowchart of the Mahony Filter algorithm can be observed in *Figure* 2.5. In this Figure, magnetometer is shown as input but the algorithm works with only accelerometer and gyroscope data as well.

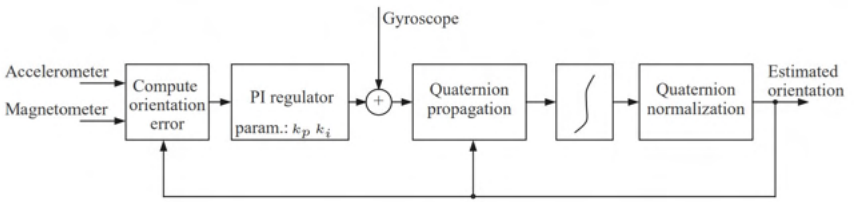

Figure 2.5 High-level overview of the Mahony Filter [Cirillo et al., 2016, Fig 1.5]

In more detail, the first step is usually to normalize the accelerometer and magnetometer measurements since only the relation of the three axes is necessary in order to determine the orientation. Since it is still based on numerical integration of the gyroscope, the Runge-Kutta method in *Equation* 2.32 is used, with quaternion state $\hat{\boldsymbol{q}}_{\boldsymbol{t}}$ at time t.

The rotation from body frame to the reference frame is different from previous methods. Instead the error from the correct estimation caused by the lack of rotation is estimated. First a frame correction vector, $\boldsymbol{v}(\hat{\boldsymbol{q}}_{\boldsymbol{t}})$, is constructed from the previous quaternion state at time $t-1$ as

$$\boldsymbol{v}(\hat{\boldsymbol{q}}_{\boldsymbol{t-1}}) = \begin{bmatrix} 2(q_2q_4 - q_1q_3) \\ 2(q_1q_2 + q_3q_4) \\ (q_1^2 - q_2^2 - q_3^2 + q_4^2). \end{bmatrix} \tag{2.33}$$

the most recent accelerometer measurements, $\boldsymbol{a_t}$, is used in order to calculate the estimated proportional orientation error $\boldsymbol{e_t}$ from the previous step

$$\boldsymbol{e_t} = \boldsymbol{a_t} \times \boldsymbol{v}(\hat{\boldsymbol{q}}_{\boldsymbol{t-1}}). \tag{2.34}$$

Furthermore, the integration error, ${}^{\boldsymbol{i}}\boldsymbol{e_t}$, is thereafter calculated as

$${}^{\boldsymbol{i}}\boldsymbol{e_t} = {}^{\boldsymbol{i}}\boldsymbol{e}_{\boldsymbol{t-1}} + \boldsymbol{e_t}\Delta t \tag{2.35}$$

where Δt is the sample period.

Next, the estimated proportional and integration error is after that added to the gyroscope measurements so that they become represented in the reference frame rather than the gyroscope's local body frame, $\boldsymbol{\omega_{corr}}$, resulting in the corrected gyroscope measurements;

$$\boldsymbol{\omega_{corr}} = \boldsymbol{\omega_t} + k_p \cdot \boldsymbol{e_t} + k_i \cdot {}^{\boldsymbol{i}}\boldsymbol{e_t}. \tag{2.36}$$

The user-defined proportional and integral constants k_p and k_i must be determined through testing, and the optimal values differ from case to case.

Lastly, the corrected gyroscope measurement is converted into quaternion space and thereafter integrated using the Runge-Kutta method as in *Equation* 2.30, 2.31 and 2.32 in order to achieve the final estimated orientation $\hat{\boldsymbol{q}}_{\boldsymbol{t}}$.

2.3.5 Madgwick Filter

A fifth proven SFA is the *Madgwick Filter* which can be modified to suite both 6-axis and 9-axis IMUs. The reason why Madgwick has shown wide recognition is that it matches high accuracy Kalman based algorithms but with lower execution time. Like Mahony Filter, it is a quaternion based algorithm, but uses an optimized *gradient descent algorithm* to determine the gyroscope measurement error instead of a PI-regulator. For the 6-axis IMU the idea is to combine integrated gyro measurements and the direction given by the accelerometer measurements. The attitude is given by integrating gyro data and attitude from accelerometer data is estimated

by using the already mentioned gradient descent algorithm. A flowchart of the algorithm can be seen in *Figure* 2.6. As with the Mahony flowchart, magnetometer is included as input but also here it could be left out.

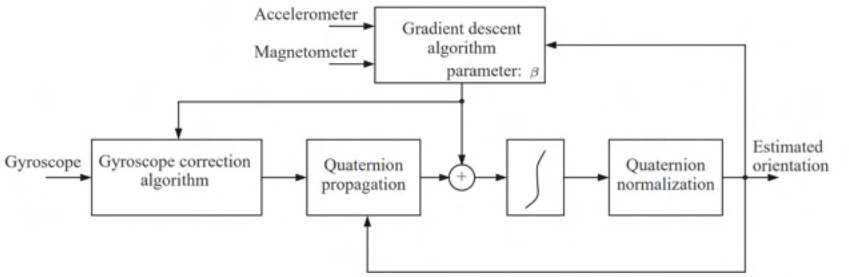

Figure 2.6 High-level overview of the Madgwick Filter [Cirillo et al., 2016, Fig 1.5]

The algorithm's target is to find the function

$$f({}^I_W\hat{\boldsymbol{q}}, {}^W\hat{\boldsymbol{g}}, {}^I\hat{\boldsymbol{a}}) = {}^I_W\hat{\boldsymbol{q}}^* \otimes {}^W\hat{\boldsymbol{g}} \otimes {}^I_W\hat{\boldsymbol{q}} - {}^I\hat{\boldsymbol{a}}, \tag{2.37}$$

and then solve the minimization problem

$$\min_{{}^I_W\hat{\boldsymbol{q}} \in \mathbb{R}^{4\times 1}} f({}^I_W\hat{\boldsymbol{q}}, {}^W\hat{\boldsymbol{g}}, {}^I\hat{\boldsymbol{a}}). \tag{2.38}$$

where prefix I indicates the inertial frame and W the world frame, see *Section* 2.2.1 for definition of frames. The hat indicates that it is a normalized vector. $\boldsymbol{q}^*$ is the conjugate of $\boldsymbol{q}$ and ${}^{\boldsymbol{W}}\hat{\boldsymbol{g}}$ a normalized gravity vector, which is $[0,0,0,1]^T$. ${}^{\boldsymbol{I}}\hat{\boldsymbol{a}}$ is the normalized acceleration measurements in the inertial frame. The filter computations follow the scheme down below.

Sampled gyroscope- and acceleration measurements are denoted ${}^{\boldsymbol{I}}\boldsymbol{\omega_t}$ and ${}^{\boldsymbol{I}}\boldsymbol{a_t}$. The acceleration measurements are normalized since only the directions are important and not the size. The new normalized acceleration vector at time t is denoted ${}^{\boldsymbol{I}}\hat{\boldsymbol{a}}_{\boldsymbol{t}}$.

The gradient step, the orientation increment, is computed as

$$\nabla f({}^I_W\hat{\boldsymbol{q}}_{est,t}, {}^W\hat{\boldsymbol{g}}, {}^I\hat{\boldsymbol{a}}_{t+1}) = \boldsymbol{J}^T({}^I_W\hat{\boldsymbol{q}}_{est,t}, {}^W\hat{\boldsymbol{g}}) f({}^I_W\hat{\boldsymbol{q}}_{est,t}, {}^W\hat{\boldsymbol{g}}, {}^I\hat{\boldsymbol{a}}_{t+1}), \tag{2.39}$$

using the acceleration measurements and the previous estimated orientation. The J function;

$$\boldsymbol{J}^T({}^I_W\hat{\boldsymbol{q}}_{est,t}, {}^W\hat{\boldsymbol{g}}) = \begin{bmatrix} -2q_3 & 2q_4 & -2q_1 & 2q_2 \\ 2q_2 & 2q_1 & 2q_4 & 2q_3 \\ 0 & -4q_2 & -4q_3 & 0 \end{bmatrix}, \tag{2.40}$$

is a 3x4 matrix and the elements of it consists of the previous estimated quaternion. The f function;

$$f({}^{I}_{W}\hat{\boldsymbol{q}}_{est,t}, {}^{W}\hat{\boldsymbol{g}}, {}^{I}\hat{\boldsymbol{a}}_{t+1}) = \begin{bmatrix} 2(q_2q_4 - q_1q_3) - \hat{a}_x \\ 2(q_1q_2 + q_3q_4) - \hat{a}_y \\ 2(\frac{1}{2} - q_2^2 - q_3^2) - \hat{a}_z \end{bmatrix}, \tag{2.41}$$

is a column vector including the previous estimated quaternion and acceleration measurements. The total update quaternion from the accelerometer measurements is calculated as

$${}^{I}_{W}\boldsymbol{q}_{\nabla,t+1} = -\beta \frac{\nabla f({}^{I}_{W}\hat{\boldsymbol{q}}_{est,t}, {}^{W}\hat{\boldsymbol{g}}, {}^{I}\hat{\boldsymbol{a}}_{t+1})}{||\nabla f({}^{I}_{W}\hat{\boldsymbol{q}}_{est,t}, {}^{W}\hat{\boldsymbol{g}}, {}^{I}\hat{\boldsymbol{a}}_{t+1})||}. \tag{2.42}$$

The filter also uses gyroscope measurements as input. The new rate of change,

$${}^{I}_{W}\dot{\boldsymbol{q}}_{\omega,t+1} = \frac{1}{2} {}^{I}_{W}\hat{\boldsymbol{q}}_{est,t} \otimes [0, {}^{I}\boldsymbol{\omega}_{t+1}]^T, \tag{2.43}$$

is calculated by taking the cross-product between the previous normalized quaternion and the gyroscope measurement. The dot above the variable indicates that it is the derivative and not a normalization, as was the case for the hat.

The quaternions are then fused to get a more accurate estimation of the attitude. The quaternions from *Equation* 2.42 and 2.43 are first added together

$${}^{I}_{W}\dot{\boldsymbol{q}}_{est,t+1} = {}^{I}_{W}\dot{\boldsymbol{q}}_{\omega,t+1} + {}^{I}_{W}\boldsymbol{q}_{\nabla,t+1}. \tag{2.44}$$

The fused measurements are then integrated,

$${}^{I}_{W}\boldsymbol{q}_{est,t+1} = {}^{I}_{W}\hat{\boldsymbol{q}}_{est,t} + {}^{I}_{W}\dot{\boldsymbol{q}}_{est,t+1}\Delta t, \tag{2.45}$$

to get a quaternion estimating the new position. In the integration Δt is the sampling time.

A convenient aspect of the Madgwick Filter compared to Mahony is that there is only one tunable parameter, β which determines the relationship between gyro and acceleration measurements. [Madgwick et al., 2011].

2.3.6 Summary of methods for attitude estimation

Several methods for attitude estimation have been presented in this chapter. Most of them apply quaternion calculations, this is an advantage since gimbal lock can be avoided. There are five different algorithms, listed below.

- Direct Tait-Bryan Angle Method

- Complementary Filter
- Factored Quaternion Algorithm (FQR)
- Mahony Filter
- Madgwick Filter

Direct Tait-Bryan Angle Method is the only one of the mentioned using trigonometric functions to calculate movement. An advantage is the simple implementation and a disadvantage is that gimbal lock can occur.

Complementary filter is a simple sensor fusion algorithm. It uses quaternions and therefore gimbal lock is avoided. Another advantage is that two sensors are fused which allows a more robust and reliable estimation of correct position since one signal can be used long-term and another one short-term. A disadvantage is that the gyroscope coordinate system have to be rotated into a reference frame to get correct measurements.

FQR also use quaternions to prevent gimbal lock but a downside is the use of a magnetometer, which is sensitive to magnetically unstable environments t and the measurements from that can not be fully trusted unless the environment is fully controlled.

Mahony Filter is according to research a highly accurate algorithm and can be seen as a PI-regulator with quaternions where the error is estimated. A disadvantage with that is that there are two parameters to tune which can be very time consuming. But the advantage is that the algorithm is easy to implement and can be very accurate when tuned properly.

Madgwick Filter is the last presented algorithm. It calculates a gradient to optimize the attitude estimation and an advantage over the Mahony is that it contains only one tuneable parameter. A disadvantage compared to Mahony is that the algorithm is harder to implement and takes more computation power.

2.4 Signal processing

MEMS-based IMUs require careful digital processing techniques to achieve an acceptable accuracy of orientation calculation, as mentioned in the previous paragraph because noise and bias accumulate when integrating the angular velocity and acceleration needed to determine the orientation.

2.4.1 Sampling data

Proper sampling is critical for a functioning system. If the sampling is too fast in a closed-loop system, the loop will lag because it is impossible to deliver data as fast

as desired and there will be redundant calculations, and if sampling is too slow, there is a risk that essential data is lost. In this case, it is crucial not to sample too slow to avoid as much drift as possible in the integration. A rule of thumb for sampling interval in a closed-loop is;

$$0.1 \leq \omega_c \Delta t \leq 0.6, \tag{2.46}$$

where ω_c is the cut-off frequency and Δt is the sampling interval [Wittenmark et al., 2002].

2.4.2 Low-Pass Filters

2.4.2.1 Simple Moving Average Common distortions of signals are noise and bias. By using calibration, bias could be removed. However, noise is a bit more complicated. It can not be accounted for in advance and, therefore, not removed from the signal. One way to account for this distortion is using a *Simple Moving-Average* (SMA) filter. The SMA-filter averages the N+1 most previous measurements from $x[n]$ as

$$y[n] = \frac{x[n] + x[n-1] + ... + x[n-N]}{N+1}. \tag{2.47}$$

where N is called the *Window Size*.

One downside with the SMA-filter is that the dynamic memory quickly grows as the window size increases. Otherwise it is an effective and simple way to reduce noise in a signal.

2.4.2.2 Exponential Weighted Moving Average An *Exponential Moving Average* (EMA) filter is an *Infinite Impulse Response* (IIR) filter that consists of exponential decreasing components. For this purpose a first-order filter have been used:

$$y[n] = \alpha x[n] + (1-\alpha) y[n-1] \tag{2.48}$$

where α is the weighting factor, $x[n]$ is the current sample and $y[n-1]$ is the previous output from the filter.

EMA-filters are similar to Simple Moving Average (SMA) filters, but the difference lies in the weighting. EMA uses more weight on the current sample and SMA is an average of the N last samples.

2.4.3 Gyroscope Bias Compensation

Several methods have been proposed to compensate for the long-term effect of gyro bias. A gyro with 0.1 dps results in 6° error after only 1 minute due to integration

drift, which is too much in order to be of any practical use. That is why gyroscopes are often combined with a magnetometer to determine the yaw over a long time accurately. However, it is still essential to reduce the long-term drift, such as when measurements are performed in unstable magnetic environments.

Since the gyroscope contains both low and high-frequency components, it is also essential to apply proper high-pass filtering to reduce DC bias and low-pass filtering to reduce noise. It is also common to introduce a threshold, ω_{thres}, such that if the gyroscope measurements, ω, is below the threshold, they are set to zero, as

$$\omega = \begin{cases} \omega & \text{if } \omega \geq \omega_{thres} \\ 0 & \text{if } \omega < \omega_{thres} \end{cases}. \tag{2.49}$$

The value of ω_{thres} must be chosen so that vibrations and noise isn't added to the integration while at the same time make sure that it is low enough to incorporate slow angular movements.

A second measure is to keep calibrating the gyroscope when it is static and to remove the bias from the output from time to time since the bias changes randomly and due to external factors such as temperature. The downside is that it disturbs the unit's operation during calibration. For example, a gyroscope sitting on a PTZ camera would not be able to rotate as the gyroscope is calibrating, which is in most cases unacceptable.

A third approach is the *Model-Based Gyro Bias Update Method* which estimates the orientation and the bias at the same time using a Kalman-based approach, thus avoiding the need for intermediate calibration. A downside of this approach is that it is more resource-heavy than the previous one. One example of such an algorithm is the approach taken by the Mahony Filter. [Fan et al., 2017]

2.4.4 Magnetometer Calibration

Cheaper magnetometers requires calibration in order to compensate for static magnetic disturbances in the surroundings originating from, for example, alternating currents or ferromagnetic objects. These disturbances can be divided into hard-iron effects and soft-iron effects.

Hard-iron effects come from permanently ferromagnetic objects on the PCB that rotate with the IMU. Therefore it demonstrates itself as a permanent bias from the origin during a 360° rotation of the magnetometer. The hard-iron effects can be calibrated by measuring the offset during a full rotation and calculate the center points, $m_{x,center}$. $m_{y,center}$, and $m_{z,center}$ that describes the offset, as

$$m_{x,center} = \frac{m_{x,max} + m_{x,min}}{2} \tag{2.50}$$

$$m_{y,center} = \frac{m_{y,max} + m_{y,min}}{2} \tag{2.51}$$

$$m_{z.center} = \frac{m_{z,max} + n_{z,min}}{2}. \tag{2.52}$$

The hard-iron calibrated magnetometer readings, $\boldsymbol{m_{hard}}$ is then calculated by subtracting the magnetometer center, $\boldsymbol{m_{center}}$, from the magnetometer readings, $\boldsymbol{m}$, to move it to origo;

$$\boldsymbol{m_{hard}} = \boldsymbol{m} - \boldsymbol{m_{center}}. \tag{2.53}$$

Soft-iron effects is a second type of magnetic disturbance that originates from normally unmagnetized ferromagnetic components that becomes induced by the geomagnetic field, such as iron or nickel for example. In comparison with hard-iron distortion, soft-iron distortion depends on the orientation relative to the interfering object. In order to compensate for this effect it is necessary to re-scale the axial response in order to make it more spherical. One simple and effective method is to use the offset measurements from *Equation* 2.50, 2.51 and 2.52 to produce the re-scaling vector $\boldsymbol{d_{soft}}$:

$$\boldsymbol{d_{soft}} = \begin{bmatrix} d_{x,soft} \\ d_{ysoft} \\ d_{z.soft} \end{bmatrix} = \begin{bmatrix} \frac{m_{x,max} - m_{x,min}}{2} \\ \frac{m_{y.max} - m_{y.min}}{2} \\ \frac{m_{z.max} - m_{z,min}}{2} \end{bmatrix} \tag{2.54}$$

with an average scaling coefficient, $\bar{d}$, of

$$\bar{d} = \frac{d_{xsoft} + d_{ysoft} + d_{zsoft}}{3}. \tag{2.55}$$

The final calibrated vector, $m_{calibrated}$, is lastly calculated by applying an averaged re-scaling matrix to the hard-calibrated magnetometer as

$$\boldsymbol{m_{calibrated}} = \boldsymbol{m_{hard}} \times \begin{bmatrix} \frac{\bar{d}}{d_x soft} & 0 & 0 \\ 0 & \frac{\bar{d}}{d_y soft} & 0 \\ 0 & 0 & \frac{\bar{d}}{d_z soft} \end{bmatrix}. \tag{2.56}$$

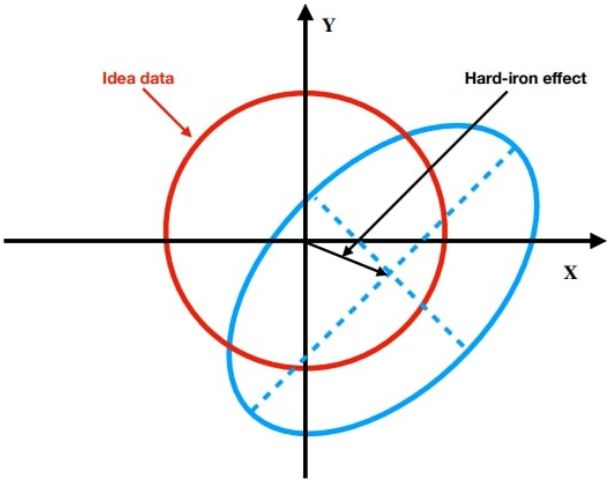

Figure 2.7 Soft and Hard Iron Effects on magnetometer measurements [Sawicki et al., 2017, Fig 3.b]

The result of soft-and hard iron effects can be seen in *Figure* 2.7.

It is important to note that the previously proposed calibration method is effective when the magnetometer rotates around its origin. Otherwise, the translation of the magnetometer's coordinate system pin relation to the surrounding magnetic coordinate system needs to be accounted for by incorporating real-time attitude estimation using the accelerometer.

3

Experimental Setup

The previous chapter presented the theoretical background needed to understand the steps of the report. This chapter presents an overview of the material used throughout the report to make it re-creatable for future researchers. *Section* 3.1 starts by presenting PTZ cameras in general and the specifications of the camera used for testing throughout the report. It continues by presenting the hardware used in the testing and finishes off with a presentation of the test setup.

3.1 Material

3.1.1 PTZ Camera

The application of replacing the existing feedback solutions with IMUs is made on a PTZ camera. The model used for this report's investigation is Axis Q6215 model provided by the company, see *Figure* 3.1 and 3.2. It has a pan range of 360° and tilt range $\pm 90°$, making it possible to cover all angles. Additionally, the zoom specifications for this camera is 30x Optical Zoom and 21x Digital Zoom. The angular velocities are limited to ± 700 dps in pan and tilt respectively.

An advantage with this model over others is that it can be tampered with in both pan and tilt. Many other PTZ cameras tilt is protected under a dome.

The Q6215 uses a magnetic encoder with a resolution of $\pm 0.005°$, see *Table* 1.1. The cost of it can be seen in Table 3.1 and is used in all camera models in the higher price range.

In the cheaper segment the camera models use a cheaper option which is an optical feedback solution. The cost of this can be seen in *Table* 3.2. The sacrifice for a cheaper solution is the resolution since the optical feedback has an accuracy of $\pm 9°$. The resolution requirements are lower in the cheaper cameras because they do not have as much zoom as the cameras in the higher price range.

Figure 3.1 Axis Q6215 camera mounted on wall facing downwards.

Figure 3.2 Axis Q6215 camera upright mounted on pole.

Source: Axis Communications AB intranet

Table 3.1 Cost of currently used magnetic feedback solution

Magnetic feedback	
2x encoder PCB	$14.18
1x metal encoder ring for pan	$6.60
1x metal ring for tilt	$6.63
Total cost	**$27.41**

Table 3.2 Cost of currently used optical feedback solution

Optical feedback	
2x PCB	$1.10
Mechanics Pan	$6.80
Mechanics Tilt	$2.98
Total cost	$10.88

3.1.2 STMicroelectronics Nucleo-G070RB

A Nucleo-64 development board with STM32G070RB MCU from STMicroelectronics is used for communication and computations. The board is provided with 16 MHz oscillator, the MCU features 128 kB memory and supports SPI and I2C. SPI is used to communicate with the IMU in this development because of speed and protocol simplicity. An argument for using a STM32 is because STMicroelectronics provides a friendly and intuitive IDE. All code is written in C.

3.1.3 InvenSense ICM20948 MEMS IMU

The *InvenSense ICM20948* Micro-electromechanical system (MEMS) sensor is used during this proof-of-concept. The chip is equipped with 9-axis motion tracking and consists of a 3-axis accelerometer, 3-axis gyroscope, and 3-axis magnetometer (compass).

3.1.3.1 3-Axis Accelerometer The accelerometer noise sensitivity is 100 µg/$\sqrt{Hz}$ with programmable Full-Scale Range (FSR) of $\pm$2 g, $\pm$4 g, $\pm$8 g and $\pm$16 g. This results in the sensitivity options 0.061 mG/LSB, 0.12207 mG/LSB, 0.244141 mG/LSB and 0.4 mG/LSB following *Equation* 3.1. Additionally, the 16-bit ADC is equipped with a number of digital low-pass filters (DLPF)

$$\rho_{step} = \frac{2 \cdot FSR}{2^{16}} / LSB. \tag{3.1}$$

3.1.3.2 3-Axis Gyroscope Likewise the gyroscope noise sensitivity is $\pm$4 mdps/$\sqrt{Hz}$ with programmable FSR of $\pm$250 dps, $\pm$500 dps, $\pm$1000 dps, $\pm$2000 dps. This results in the sensitivity options 0.0076 dps/LSB, 0.0153 dps/LSB, 0.03048 dps/LSB and 0.608 dps/LSB. Additionally, the sensitivity error of the gyroscope is $\pm$ 1%. Both the accelerometer and gyroscope data are fetched from a 16-bit ADC with a set of optional digital filters.

3.1.3.3 3-Axis Magnetometer A magnetometer is a correct term for a compass. The range of ICM20948s magnetometer is $\pm$4900 μT and has a sensitivity of 0.15 μT/LSB. No information about the magnetometer noise is present in the datasheet.

3.2 InvenSense ICM20602 MEMS IMU

The *ICM20602* MEMS IMU comes from the same manufacturer as the *ICM20948* mentioned above. The difference between the two is that the ICM20602 does not have a magnetometer included. The ICM20602 is a bit cheaper and is thus a good alternative if there is no need for a magnetometer.

3.3 Cost of IMUs

Table 3.3 presents the cost for the two IMU models used in this master thesis. The stated prices are per unit when ordering 1000 units at *DigiKey* which is a frequently used supplier to Axis.

Table 3.3 Cost of used IMU models

ICM20948	$5.50
ICM20602	$2.40

3.4 Test Environment

The initial test setup can be seen in *Figure* 3.3. 1) is the *STM32*, 2) slip ring connecting the micro-controller with the IMU to prevent the cables from tangling when rotating., and 3) the IMU. The ICM20948 is temporarily placed with its x- and y-axis in horizontal on the part of the camera, which can only rotate in pan. If the concept were to be integrated into the camera, the IMU would be placed in a more suitable location. Nevertheless, it is a convenient place for measuring yaw angle for now and it fulfills the criteria for the first problem discussed in *Section* 1.2.

In *Figure* 3.4 the second test setup can be seen. The micro-controller and the slip ring are placed as before. However, the IMU is now located so it can rotate both in pan and tilt. This scenario is the second problem formulation in *Section* 1.2. The first

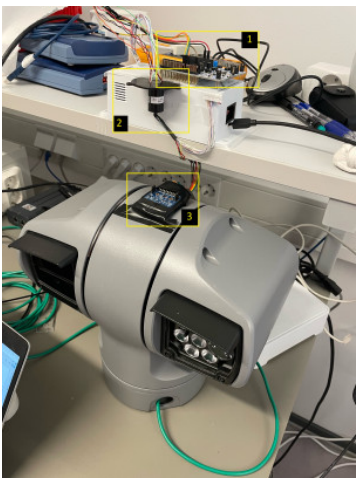

Figure 3.3 Pan Test Setup using the Axis Q-6215 PTZ camera.

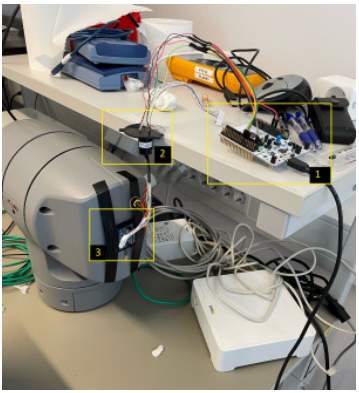

Figure 3.4 Tilt Test Setup using the Axis Q-6215 PTZ camera.

problem formulation was only to get started with the measurements and get familiar with the environment. This setup is the real challenge to get accurate measurements since the IMU can rotate in both pan and tilt. *Figure* 3.5 shows a setup when testing reliability of magnetometer using a permanent disturbance in the form of a wrench.

Figure 3.5 Setup when testing magnetometer with disturbance present.

4

IMU Measurements

This chapter explores the functions and constraints of the IMU to achieve the main aim of the thesis. *Section* 4.1 evaluates the impact of gyroscope bias, *Section* 4.2 presents the impact of acceleration noise, and *Section* 4.3 explores the quality of the magnetometer signals.

4.1 Gyroscope Bias

Figure 4.1 shows the gyroscope bias for rotation around the z-axis (yaw) with different DLPF settings sampled at 50 Hz over one minute after initial bias calibration with a resolution set to ± 1000 dps. The result was similar for the other two axes, so only one result is shown.

The initial bias calibration is done by averaging 1000 samples as the gyroscope lies idle at start. This value is subtracted from each axis. The calibration accuracy depends on the resolution configured on the gyroscope - the better resolution, the better calibration. It is clearly seen that the drift increases linearly with around 35° per minute when no filter is applied. The digital low-pass filter on the IMU has a significant impact in dealing with drift caused by the gyroscope bias and achieves a drift of fewer than 1° per minute in idle state, see *Figure* 4.2. This Figure shows the same measurements but without the one labeled “No filter" (12106 Hz)” in *Figure* 4.1 to see the other results better. Small vibrations in the testing environment also help build up the bias, explaining why the filters perform differently. However, it is evident that filters with the lowest cut-off frequencies, 11.6 Hz and 5.7 Hz, perform best.

Furthermore, the filter with a cut-off frequency of 196.6 Hz seems to perform well with a low bias according to *Figure* 4.2. However, the drift is difficult to control with the gyroscope alone in the presence of vibrations. Therefore, additional calibrations might be needed to determine orientation over time with a gyroscope.

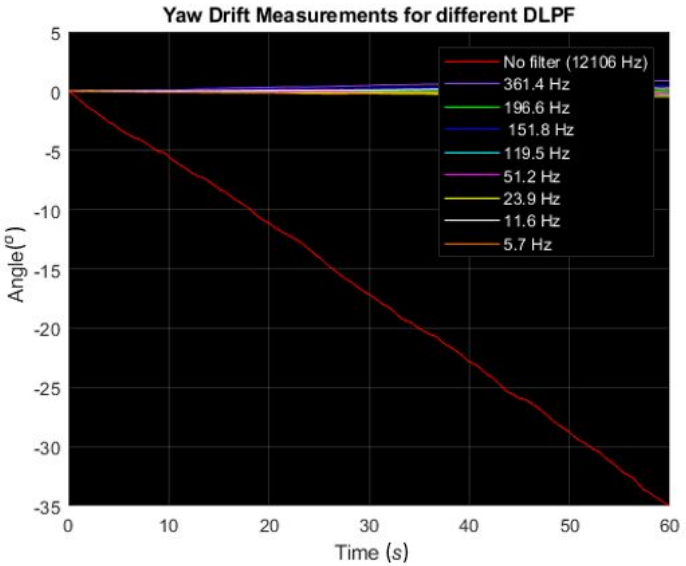

Figure 4.1 Measurements of the yaw drift for a variety of DLPFs, with the 12106 Hz filter included.

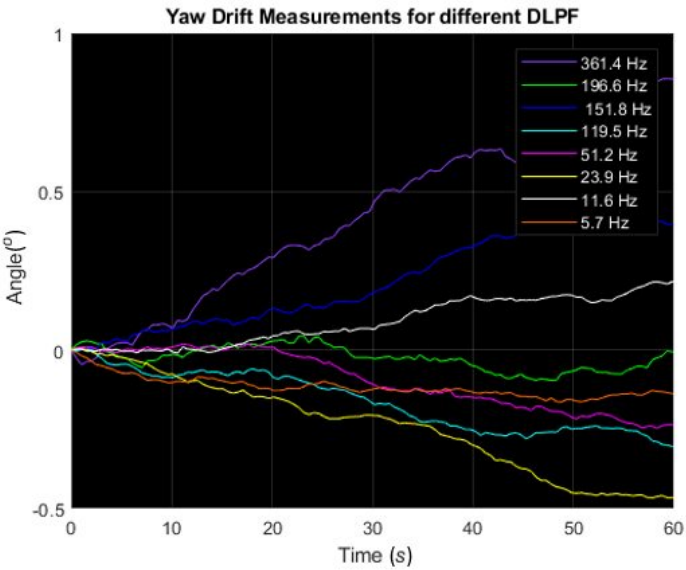

Figure 4.2 Measurements of the yaw drift for a variety of DLPFs in more detail,with the 12106 Hz filter excluded.

4.2 Acceleration Noise

Figure 4.3 shows the accelerometer noise for the z-axis for different DLPF settings sampled at 10 Hz over 10 seconds after initial calibration with a resolution set to ± 8 g. The noise is only shown for one axis but is similar for the other two. As expected, less noise is present in the lower cut-off frequency in the DLPF that is used. With the highest cut-off frequency, using DLPF (1046 Hz), an unacceptable amount of noise can be seen. In this case, as in most, the less noise, the better. But noise is however expected from accelerometers as discussed in *Section* 2.2. Yet, using filters from 21,2 Hz and below results in noise levels below 0,001 g (approximately 0,01 m/s^2) which can be accepted in this case.

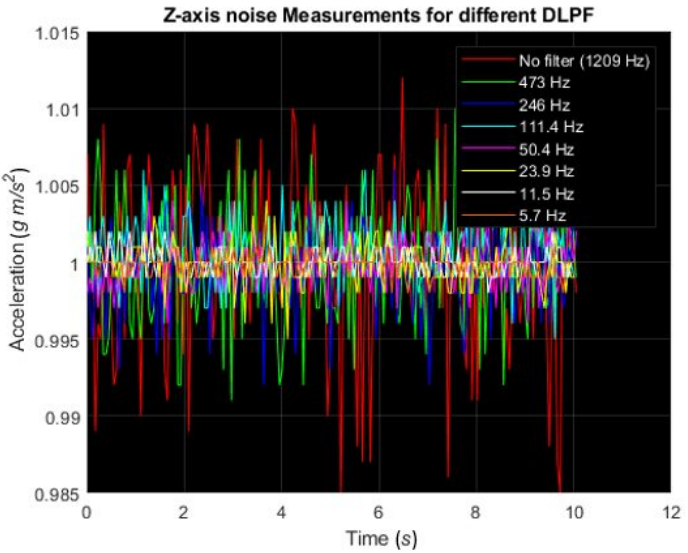

Figure 4.3 Measurements of accelerometer noise with different DLPFs applied.

4.3 Magnetometer Disturbances

The magnetometer measurements were sampled with 50 Hz while rotating around z-axis 360°. Four tests were conducted with the results seen in *Figure* 4.4 and they were taken during different magnetic conditions in order to demonstrate the effects of magnetic disturbances in the environment. For three of the four tests the setup in *Figure* 3.3 were used and for the final test the setup in *Figure* 3.5 were used.

A moving average filter with a window size of 10 was used to get rid of some of the noise that was evident while reading raw data. The difference by applying this

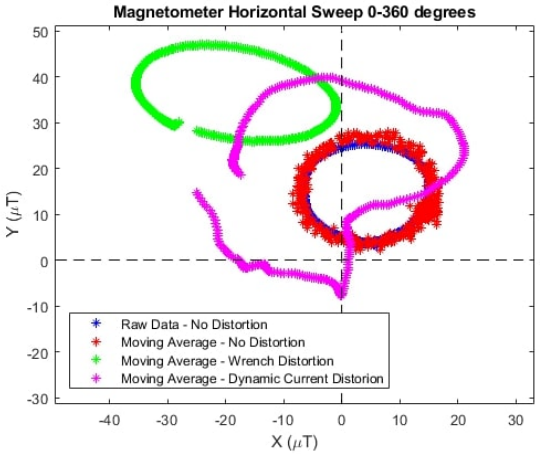

Figure 4.4 Plot shows magnetometer field strength in x and y as it is rotated 360° in pan (horizontally): without moving average, with moving average and no distortion, with moving average and fixed magnetic distortion, and with moving average and dynamical magnetic distortion.

filter can be observed by comparing the red circle with the blue circle in *Figure* 4.4. However, with the filter comes a delay, which makes it not suitable for faster signals. Nevertheless, the magnetometer was not intended to be used in this way but only considered to complement the more precise gyroscope.

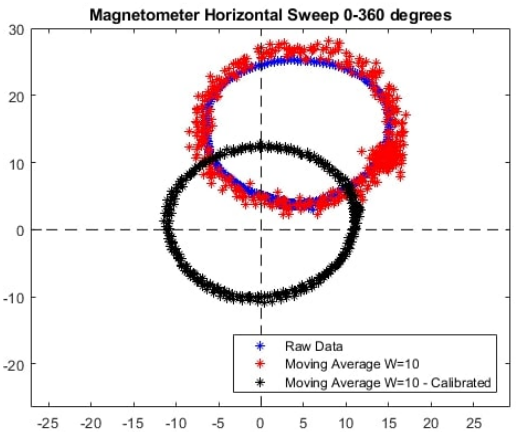

Figure 4.5 Impact of soft-and hard-iron calibration in combination with SMA low-pass filter.

Furthermore, *Figure* 4.4 shows how the magnetometer is affected by both dynamic and static magnetic fields. The static field was produced by fixing an iron wrench about 3 cm from the IMU and is seen in the stretched green curve, and the dynamic field was produced by holding the 90 W midspan which was supplying power to the camera around 5-10 cm during the sweep and is seen in the pink curve.

The magnetometer is sensitive to external magnetic fields, which drastically degrade the performance of using it to determine yaw orientation by using the magnetic field of the earth as a reference. Nonetheless, there are both hard and soft iron effects on the readings during normal office circumstances as well. The results of applying hard and soft iron compensation according to the method described in *Chapter* 2.4.4 can be seen in *Figure* 4.5. It is still evident that the performance of the magnetometer after calibration is far from perfect.

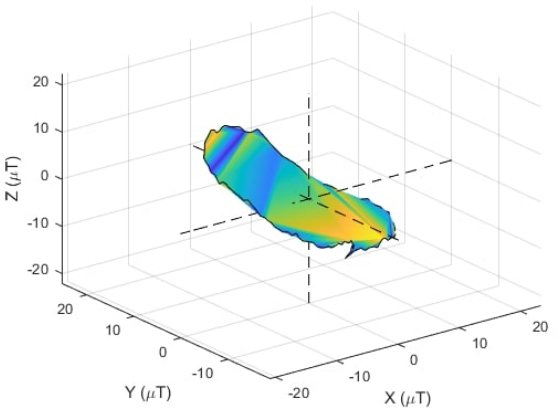

Figure 4.6 3D plot of magnetometer field strength as it is rotated 360° in pan (horizontally), sampled at 50 Hz without SMA low-pass filter.

Additionally, the 3D effects of hard and soft compensation with and without moving average filter during calibration and measurement can be seen by comparing *Figure* 4.6 and 4.7. The filter increases the performance of the magnetometer readings. Nonetheless, the results are far from a perfect circle along the x-y plane with its center in origo. Additional measures are evidently needed in order to get reliable results. As noted at the beginning of the chapter, all measurements have been performed in an indoor office environment. Therefore, it is not determined how well the magnetometer performs in outdoor conditions. Nonetheless, additional measures are needed if it were to be used in a camera that is expected to function correctly during all kinds of environments - indoors in a factory environment with large machines or on the sea or near high power cables. For example, more sophisticated

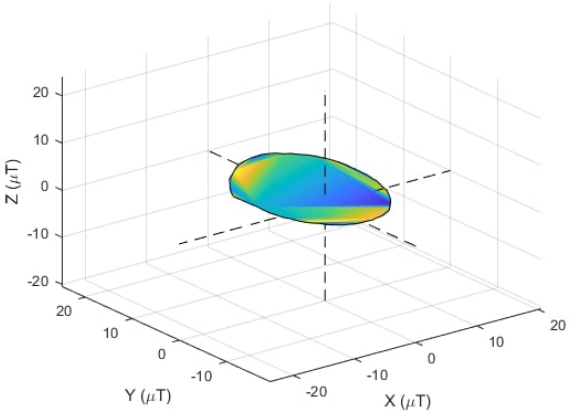

Figure 4.7 3D plot of magnetometer field strength as it is rotated 360° in pan (horizontally), sampled at 50 Hz with SMA low-pass filter using N=10.

calibration techniques and noise detection algorithms could help increase the performance. The purpose of the implementation is to make it as general as possible which means it needs to function properly in any environment with disturbances. It has therefore been decided not to use the magnetometer because of its unreliability.

5

Testing & Evaluation

This chapter will dive deeper into the IMU as a tampering detection and correction mechanism for PTZ cameras. More precisely, the possibility of achieving accurate orientation measurements is explored through four testing fields. *Section* 5.1 evaluates the quality of the IMU as an angle sensor when the rotation is fixed on one axis. *Section* 5.2 evaluates the performance of two different Sensor Fusion Algorithms. Additionally, to understand the robustness requirements of the IMU, *Section* 5.3 evaluates the impact of tampering on the camera, and lastly *Section* 5.4 measures the impact of vibrations through real-world field testing.

5.1 Fixed Axis

5.1.1 Pan Result

Fixed axis pan testing was performed using the setup shown in *Figure* 3.3 by placing the IMU on the camera with its x- and y-axis in horizontal position and comparing with the magnetic encoder as reference. The gyroscope offset was subtracted before the measurements were performed by averaging the first 1000 samples. Additionally, a threshold of ± 0.3048 dps was used to eliminate errors caused by small vibrations. It is important to stress that this value was determined as a trade-off between vibration resistance and resolution. Therefore, it is not guaranteed to perform likewise in environments with more vibration.

Figure 5.1 shows the squared yaw angle error with two different angle measurement methods. The red curve shows the squared error when using Tait-Bryan angles for gyro measurements using numerical integration with a sample time of $T_s = 20$ ms. The blue curve shows the squared error when using the Runge-Kutta quaternion estimation described in *Equation* 2.30, 2.31 and 2.32.

The two methods for calculating angle from gyro shows a substantial difference. When using Tait-Bryan angles, the error diverges. However, when using quaternions, the error stays at a level below 1°. *Figure* 5.2 shows the same measurements

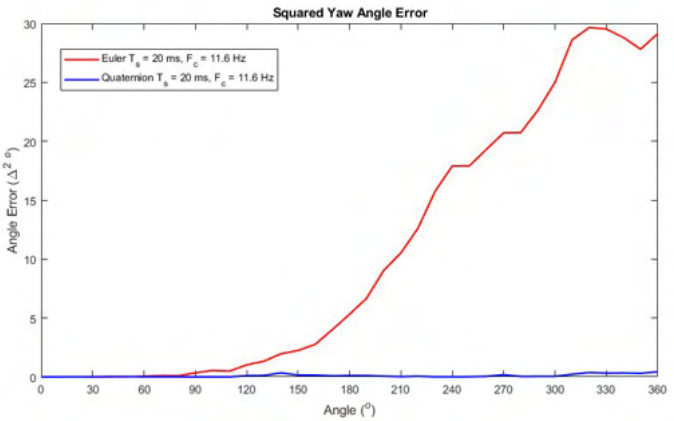

Figure 5.1 Squared yaw angle error between gyro and magnetic encoder with direct integration (red) and Runge-Kutta quaternion integration (blue).

as the blue curve in *Figure* 5.1 in better detail. A different scale on the y-axis gives a better perspective on the error when using quaternions; when turning 360°, the squared error, and hence the error, is less than 1°.

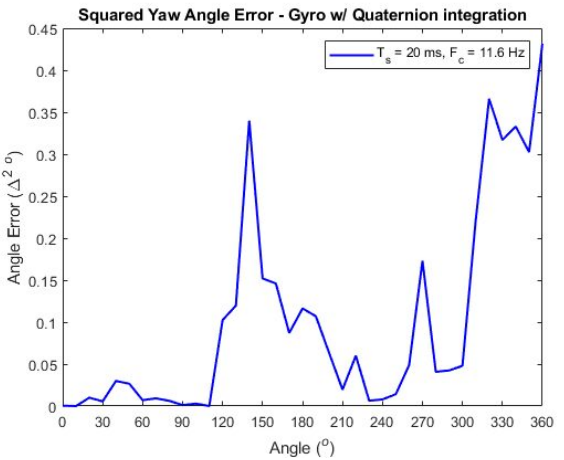

Figure 5.2 Squared yaw angle error between gyro and magnetic encoder for Runge-Kutta quaternion integration in more detail.

5.1.2 Tilt Result

Using the setup shown in *Figure* 3.4 by placing the IMU on the side of the camera with its x-and y-axis in the vertical position, it was possible to compare the IMU performance with the magnetic encoder. Similarly, as in the pan result, a threshold of ± 0.3048 dps was used to eliminate vibration errors accumulated by the gyroscope integration. Additionally, low-pass filters were applied to both the accelerometer and the gyroscope to reduce noise. Lastly, an average of 1000 initial pitch and roll angles samples was determined as an offset and subtracted from all angle readings to account for the IMU not being placed perfectly along the vertical axis.

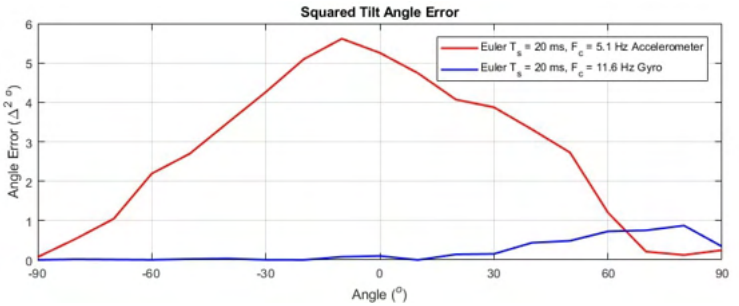

Figure 5.3 Squared tilt angle error between both gyro and accelerometer.

Figure 5.3 shows the squared roll angle error compared with the magnetic encoder; the accelerometer in red and of the gyroscope in blue. The gyroscope shows desirable short term performance with a quadratic error below 1°, but where the error increases slightly at the end of the test, suggesting drift, as could also be seen at the end of the gyroscope yaw measurements in *Figure* 5.2. However, the gyroscope angle error is slightly more prominent in the tilt measurements than in the yaw measurement, caused by the fact that external vertical vibrations are more profound than horizontally. A more aggressive vertical threshold could be needed if the gyroscope determines the tilt-angle alone. A better way would be to fuse it with the accelerometer in an SFA.

The gyroscope performance nonetheless shows better short-term performance than the accelerometer, in which the error is biggest around 0° and smallest around 90° and -90°. It could be the effect of factory calibration parameters that changes slightly after thermal stress during the soldering process, which in turn suggests that re-calibration could be necessary to achieve more accurate results around 0° [Pedley, 2015].

5.2 Sensor Fusion Algorithm

There are different types of sensor fusion algorithms for both rotation and filtration. *Section* 2.3 mentions the Complementary filter, Mahony filter, FQA, and Madgwick, yet, there are many more. We have chosen to look into Mahony and Madgwick in more detail. The reason for not testing more algorithms is lack of time and the similarity in results compared to, for example, Kalman Filter and FQA [Ludwig and Burnham, 2018].

As described in *Section* 2.3.4, the Mahony filter is a PI-controller with one integration constant and one proportional constant that tunes the performance depending on the use case. Testing is vital when deciding on the two parameters.

Using the settings in *Table* 5.1, a reasonable low error was given. The two filters underwent two different tests - *Continous* and *Sweep*. The first results in *Section* 5.2.1 show the continuous measurements with different tilt and pan angles with no calibration in between any of the measurements. The second test results in *Section* 5.2.2 show the sweep measurements, where after every measurement, the camera resets to yaw angle 0° and tilt angle 90° for calibration before the next measurement. The results demonstrate the error against the magnetic encoder as a “true” reference and is split into two tests to evaluate the performance of having the algorithm running continuously or by only using it to measure relative estimation differences.

Table 5.1 Mahony Filter parameters

f_s	50 Hz
K_p	0.4
K_i	1.1

The Madgwick filter uses only one parameter compared to the Mahony filter that uses two. The optimal parameter was found through testing and comparing the attitude estimation with the magnetic encoder and is shown in *Table* 5.2. In the evaluation of the two algorithms, the same sampling frequency was used.

Table 5.2 Madgwick filter parameters

f_s	50 Hz
β	0.1

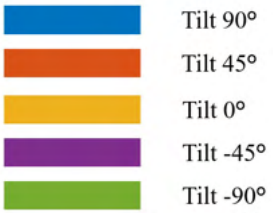

Figure 5.4 Color labels of tilt angles for *Figure* 5.5, 5.6, 5.7, 5.8

5.2.1 Continuous Measurements

The continuous filter measurements were performed by first calibrating the gyroscope offset with 1000 samples when the IMU was idle. In addition, an exponential weighted moving average low-pass filter with $\alpha = 0.2$ was applied to the gyroscope data to reduce noise. Furthermore, the proportional and integral parameter for the Mahony filter and the gain parameter, β, for Madgwick Filter was chosen as in *Table* 5.1 and 5.2, after experimental testing for a subjective optimal value in a test environment. Additionally, a rotation matrix was applied to the acceleration measurements to correct for misalignments in pitch and roll.

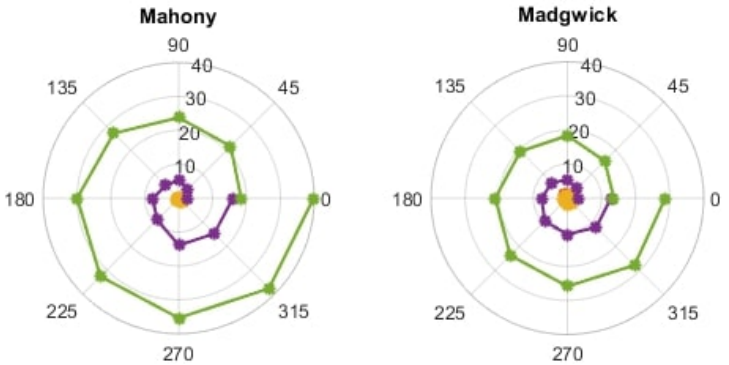

Figure 5.5 Continuous Pan Error between reference (magnetic encoder) and IMU for Pan $0° - 360°$ and Tilt $90°$, $45°$, $0°$, $-45°$, and $-85°$

The Pan angle error is shown in *Figure* 5.5. It demonstrates the failure of the gyroscope to estimate the pan (yaw) angle over time because of accumulated errors for both filters. However, it is not until the fourth turn at -45° that the estimation begins to drift considerably as the first 360° rotation shows promising results with low errors. At the end of the last 360° rotation at -90° tilt, the accumulated error has grown to approximately 40° for Mahony and 30° for Madgwick, which indicates that Madgwick has better bias compensation performance over time. Nonetheless, both filters show bad performance over time, making them unusable in an applica-

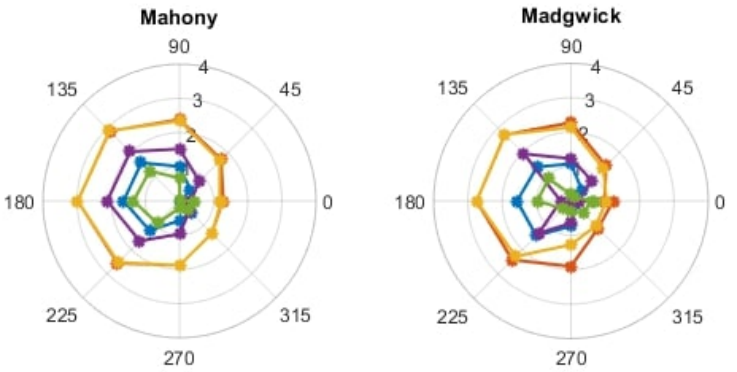

Figure 5.6 Continuous Tilt Error between reference (magnetic encoder) and IMU for Pan $0° - 360°$ and Tilt 90°, 45°, 0°, −45°, and −85°

tion like this without any additional reference.

Furthermore, the tilt angle error in *Figure* 5.6 shows varied performance along with the tilt angle range with the best performance at 0°, -45° and -90° and worst performance at 45° and 0° for both filters. The result is expected compared with the fixed accelerometer tilt result in *Figure* 5.3 and may be a result of poor accelerometer calibration. The angle error is smaller than if the accelerometer were to be used alone since the gyroscope has good short-term performance and the accelerometer has good long-term performance. The drift can therefore be eliminated while at the same time providing desirable accuracy. This is not the case in pan since the accelerometer cannot measure the yaw angle and cannot be fused with to compensate for drift as it can in tilt.

5.2.2 Sweep Measurements

As seen in the previous section, continuous measurements did not give accurate position feedback because of the drift, which is unavoidable during integration. The second sweep test avoids it by not integrating continuously. The same initialization procedure was used for the sweep measurements by calibrating the gyroscope by measuring the offset of 1000 samples with the IMU in an idle position. The same exponential moving average filter with $\alpha = 0.2$ was also applied to reduce noise. The other parameters were also the same as in the first continuous measurements in order to achieve a fair comparison, see *Table* 5.1 and 5.2.

Figure 5.7 shows the pan angle error between the IMU and magnetic encoder when using the sweep method. When applying the Mahony Filter the maximum error occurs when tilting 180° (from idle position which is tilt 90° to -90°), then the error is approximately 4°. For the Madgwick Filter the error goes up to approximately 3.5° when tilting to -45° and pan to 270°. When comparing to the continuous mea-

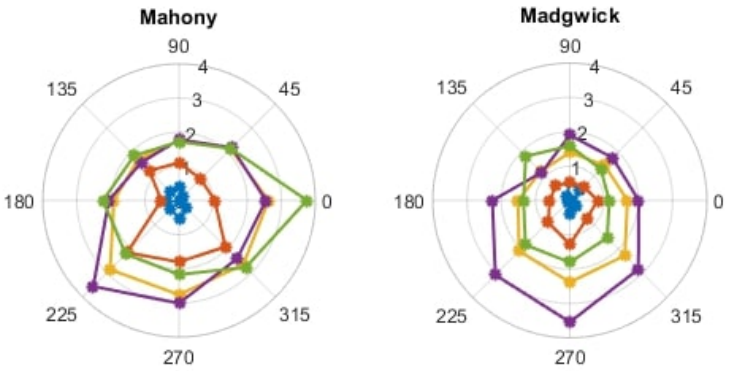

Figure 5.7 Sweep Pan Error between reference (magnetic encoder) and IMU for Pan 0° − 360° and Tilt 90°, 45°, 0°, −45°, and −85°

surements in *Figure* 5.5 there is a significant difference in the errors. The errors are almost a factor of 10 larger for the continuous measurements. It is because the errors accumulate as the integration progresses continuously. When using the sweep method, only the camera's movement is integrated, which can be achieved with the help of a threshold. If the gyroscope and accelerometer measurements exceed the threshold, integration will progress, and the accumulated error can reduced. The threshold might have to be adapted to the environement that it is used within. Suppose it is used in an environment with considerable vibration. In that case, a low threshold might not be enough to minimize the accumulated errors. Using it instead in a stable environment, then a big threshold might negatively affect the orientation estimation. In summary, a suitable threshold requires testing in different environments.

Figure 5.8 shows the tilt error for both filters when using the sweep method. With the Mahony filter there is a maximum error of approximately 3° for tilt 0° and 45° and pan 180°. The Madgwick filter shows a similar error for the same angles. Comparing these results with the continuous measurements does not differ significantly because of the fusing between gyroscope and accelerometer. It gives a more accurate position estimation than when the gyroscope measurements are used alone, as is the case for pan. When fusing, the gyroscope can be used for short-term changes and the accelerometer for long-term, leading to a low accumulated error and reduced drift.

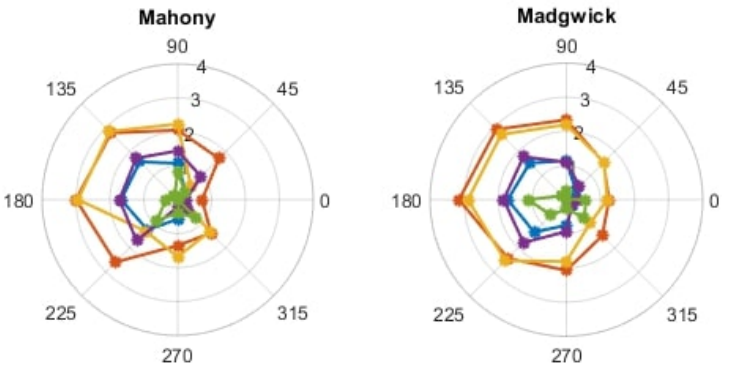

Figure 5.8 Sweep Tilt Error between reference (magnetic encoder) and IMU for Pan 0° − 360° and Tilt 90°, 45°, 0°, −45°, and −85°

5.2.3 Error Interpolation

Since the encoder acts as feedback that the testing can be bench-marked against, it can also be used for calibration by examining and interpolating the error profile for pan and tilt. *Figure* 5.9 shows an interpolation surface of the pan angle error (yaw) as a function of tilt and pan angle for both Mahony and Madgwick. *Figure* 5.10 shows tilt angle error as a function of tilt angle and pan angle of both filters likewise. A polynomial $f(\psi, \varphi)$ was interpolated to the measurement error using the *Surface Fitting* functionality from MATLAB's *Curve Fitting Toolbox* [MATLAB, n.d.]

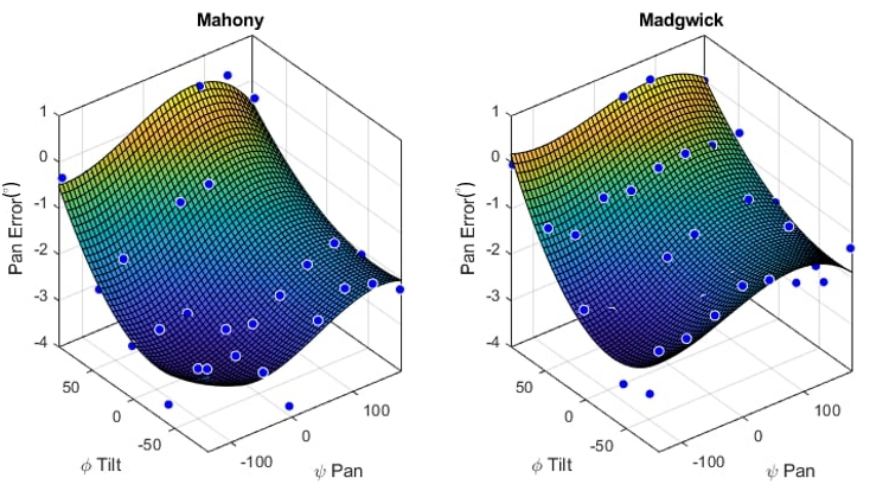

Figure 5.9 Interpolation surface of the pan angle error (yaw) as a function of tilt angle and pan angle.

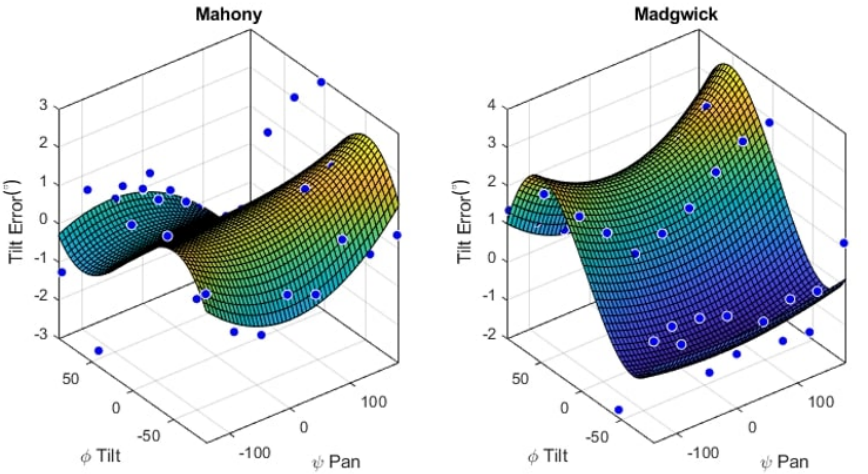

Figure 5.10 Interpolation surface of the tilt angle error (roll) as a function of tilt angle and pan angle.

As can be seen in *Figure* 5.10, Madgwick shows a more pleasing error trend that is easier to interpolate than Mahony, which may be an indication that the Madgwick Filter is more robust than the Mahony Filter. The pan error in *Figure* 5.9 however demonstrates a similar profile.

The interpolated surface can be seen as a calibration surface that depends on systematic and random errors of the IMU. With the interpolation's error estimation, it is possible to get even more accurate measurements from both filter's estimations of the angles and hence get a more accurate orientation. From empirical results, it is evident that minor alignment differences between the IMU's x-axis and the axis of the camera have a profound impact. However, this error is expected to be very small as the IMU is mechanically integrated into a camera. Nevertheless, it would still need to be re-calibrated for each unit after production to account for factory errors.

5.3 Tampering Measurements

One of the scopes of this thesis is to detect and compensate for tampering in both pan and tilt. In order to configure the system, it is desirable to measure the difference between regular motor movements - as the motor is told to move from home position (0°) to 90°-and when the system has been tampered with. In *Section* 2.1 it was mentioned that in many cases, a hold current is present in the step motors, which creates a slight resistance in tampering. These measurements are conducted to detect

a significant difference in gyroscope and accelerometer data when the hold current is counteracted.

Figures 5.11, 5.12, 5.13 and 5.14 show plots of gyroscope measurements and acceleration measurements for non-tampering movements and tampering attempts in pan (yaw). In all *Figures* the left plots show data for expected movements 90°, and the right plots show tampering attempts. *Figures* 5.15, 5.16, 5.17 and 5.18 show the same kind of measurements but in tilt. Five measurements were done in the case with expected movement and eight measurements were done in the tampering case with various velocities to get a wide profile.

5.3.1 Pan Measurements

Figure 5.11 shows two plots of gyroscope measurements in yaw (z-axis). The left plot shows angular velocity when movement is expected 90°, and the right plot shows angular velocity when approximately 90°. The tampering velocities are in the range of approximately 50 dps and 320 dps. A recurrent pattern can be seen in the left plot with expected movements and the maximum velocity is the same for all measurements, approximately 150 dps. The angular acceleration also has a recurrent pattern between measurements, which can be concluded from similar velocity increases. The right plot with tampering measurements is less correlated with each other, and they differ a lot depending on the strength of the tampering.

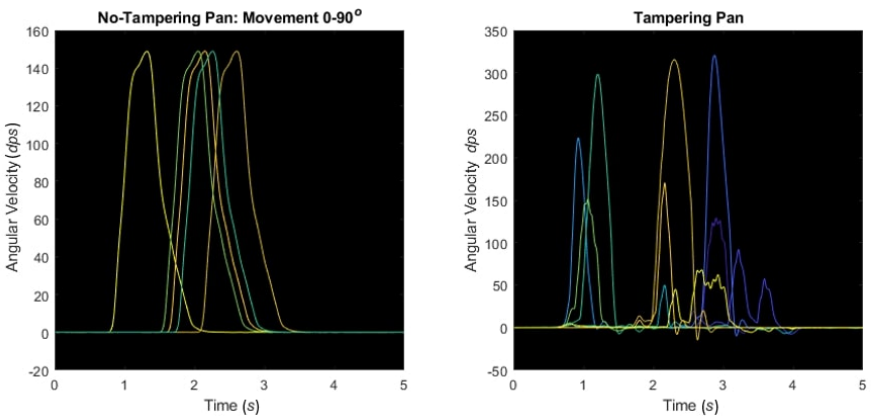

Figure 5.11 Left picture: angular velocity in pan (yaw) when the camera is moving as planned 90°. Right picture: angular velocity when tampering in pan.

Figure 5.12 shows x-axis acceleration for the same measurements. Also, here a pattern in the expected movements can be seen. The acceleration is approximately maximum 0.08 g for all measurements, and the peaks have a similar appearance. There is an initial negative acceleration for some of the measurements, which could

be due to worn-out mechanics in the test camera. There is no obvious pattern for the tampering case because of the variety in strength of the different tampering attempts.

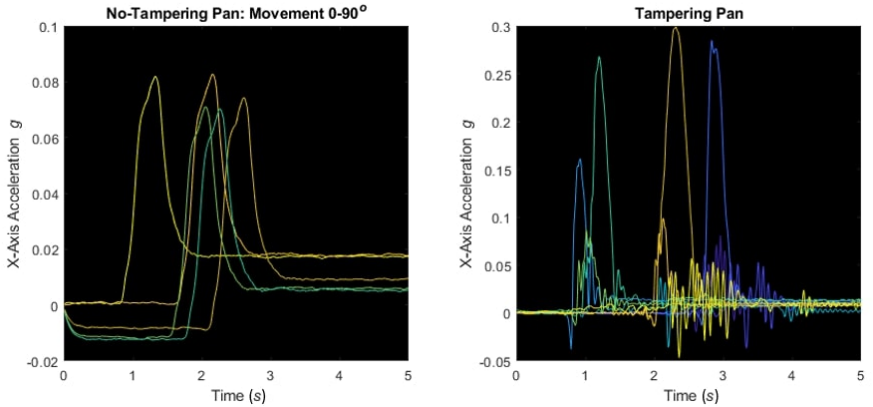

Figure 5.12 Left picture: x-axis acceleration when the camera is moving as planned 90°. Right picture: x-axis acceleration when tampering in pan.

Figure 5.13 shows y-axis acceleration for the measurements. The left plot shows acceleration when the camera moves 90° as expected and have a pattern that is easy to recognize both for positive and negative accelerations. The absolute value of the maximum is approximately 0.1 g, both positive and negative since acceleration starts from 0° and retardation when close to 90°.

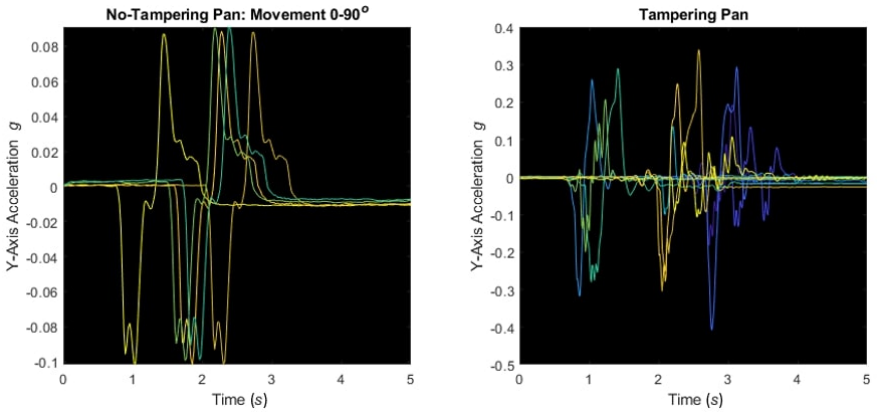

Figure 5.13 Left picture: y-axis acceleration when the camera is moving as planned 90°. Right picture: y-axis acceleration when tampering in pan.

Figure 5.14 shows the z-axis acceleration when camera is moving. Since the camera is placed with the z-axis in the vertical position, it is expected that when the camera is idle, then the acceleration is 1 g. In the left plot, depending on when the movement started in the recording, the deviations from 1 g comes at different times, but a pattern can be seen in the peaks of the deviations. There are no recognizable patterns in the right plot, showing the tampering attempts.

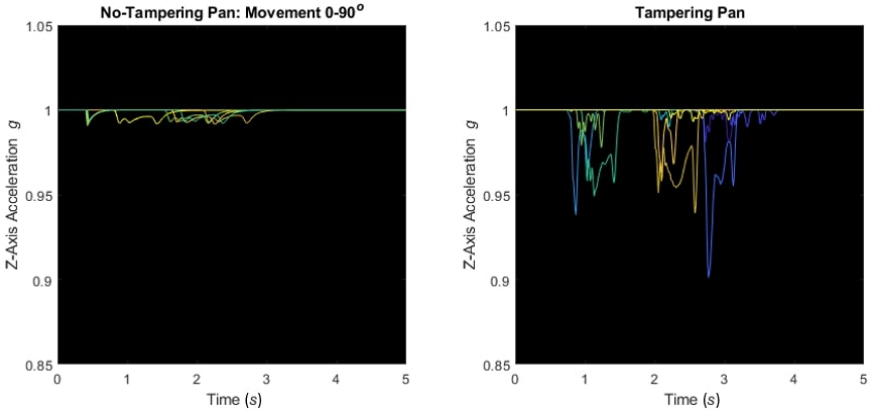

Figure 5.14 Left picture: z-axis acceleration when the camera is moving as planned 90°. Right picture: z-axis acceleration when tampering in pan.

The reason that the different axis accelerations have their behavior is because of the placement of the IMU. When testing, the placement had the x- and y-axis aligned with the horizontal axis, and the z-axis aligned with the vertical. If the concept is integrated into a camera, the IMU might have another orientation in its placement. Then it is crucial to have a factory calibration process in place.

5.3.2 Tilt Measurements

Figure 5.11 shows the difference in pan and *Figure* 5.15 shows the difference in tilt for five normal movements and eight tampering movements. The tampering movements were as small as possible and with much force to include the full range of possible tampering profiles. The pan measurements show the z-axis (yaw) angular velocity, and the tilt measurements show the x-axis (roll) angular velocity.

The figures show that the IMU experiences approximately 150 dps in both pan and tilt during a meant movement configured at the fastest speed on the Axis Q6215 model. A high of approximately 325 dps and a low of approximately 50 dps are seen in the pan tampering movements, and a high of approximately 400 dps and a low of approximately 125 dps are seen in tilt. Regular movements take an average of 0,48 s until it reaches their maximum in pan, whereas tampering takes 0,40 s. In tilt, regular movements take an average 0.57 s until they reach their maximal angular velocity,

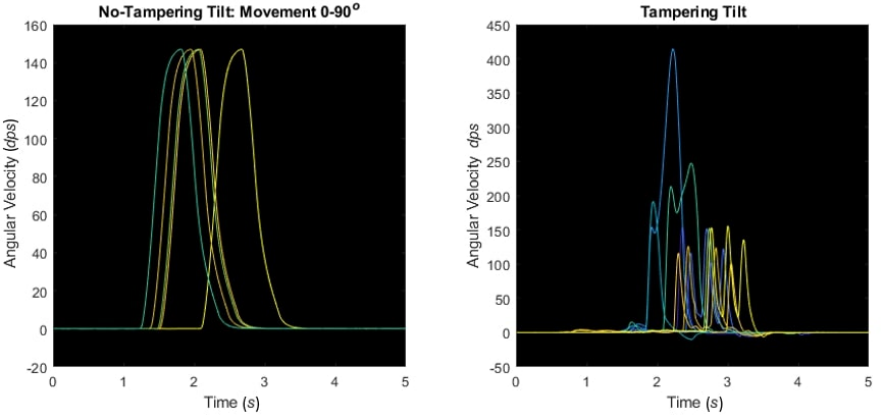

Figure 5.15 Left picture: angular velocity in tilt when the camera is moving as planned 90°. Right picture: angular velocity when tampering in tilt.

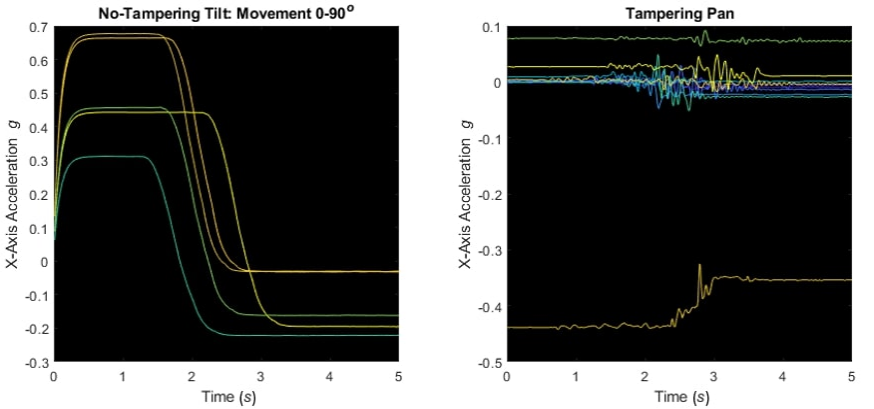

Figure 5.16 Left picture: x-axis acceleration when the camera is moving as planned 90°. Right picture: angular velocity when tampering in tilt.

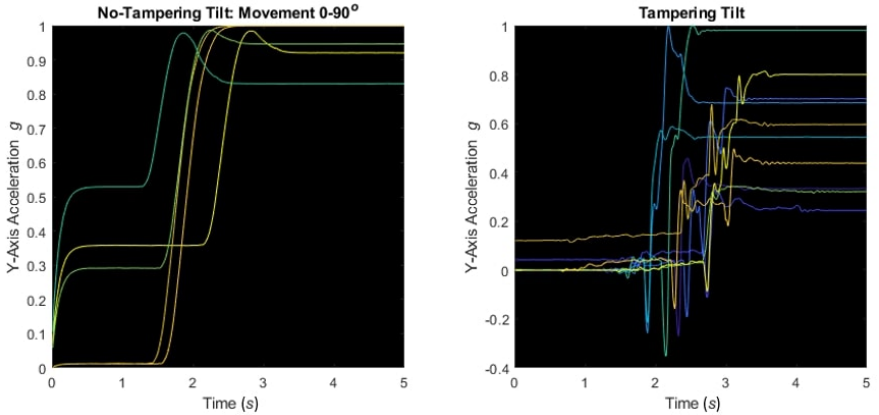

Figure 5.17 Left picture: y-axis acceleration in tilt when the camera is moving as planned 90°. Right picture: angular velocity when tampering in tilt.

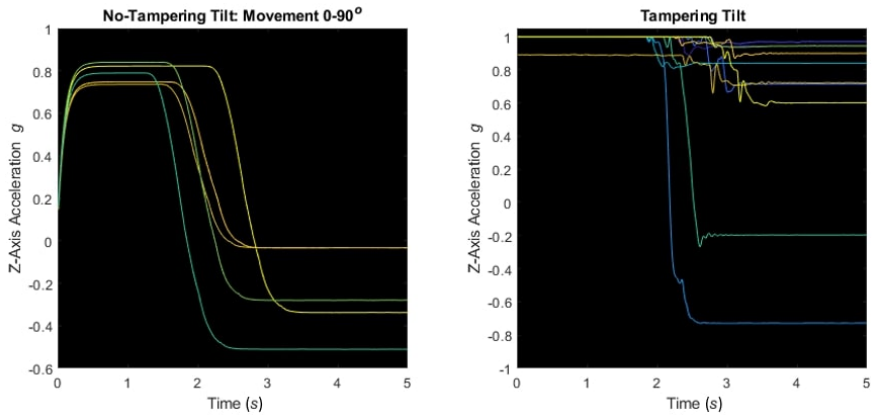

Figure 5.18 Left picture: z-axis acceleration in tilt when the camera is moving as planned 90°. Right picture: angular velocity when tampering in tilt.

whereas tampering movements take 0.32 s. Tampering in tilt, therefore, experiences higher velocities and higher angular accelerations that ought to be easier to detect. Therefore, it is possible to detect tampering movements, primarily if it is known in software that the camera should not be moving.

It is worth mentioning that the difference in pan and tilt also depends on the slack in the motor belts, which affects the impact of glitches. Therefore, a new tight motor belt camera would have been expected to show even higher, more accurate tampering measurements. Since the camera tested has experienced many tampering attempts, it suffers from deteriorated mechanics.

5.4 Vibration Measurements

It is most common for Axis PTZ cameras to be mounted on a fixed surface, such as a roof or wall, but nothing prevents them from being mounted on moving objects. A client may want to mount it on, for example, a shipping boat, on the trunk of a pick-up car, or at the top of a crane, which in turn means that any solution would need to be able to handle vibrations from such applications. In order to quantify such vibrations, the camera used for testing was fastened in the trunk of a car as can be seen in *Figure* 5.19 after which each IMU axis was measured during a long 10 minute route and a short 1 minute route, shown in *Figure* 5.20. The long route, A to B, included longer angular motions, such as those experienced in round-a-bouts, and short motions caused by bumpy roads. The short route, C to D, was included to measure the impact of speed bumps.

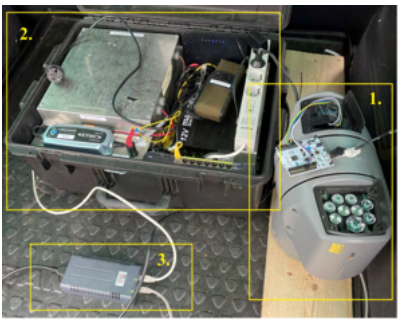

Figure 5.19 Vibration test setup in the trunk of a Volkswagen Touran. 1) Axis Q6215, 2) Power box, 3) 90W midspan.

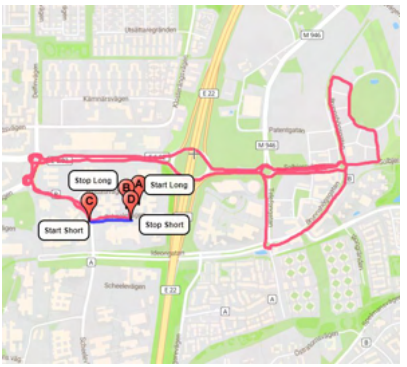

Figure 5.20 Map showing long and short vibration test route.

The short route acceleration measurements in *Figure* 5.21 shows expected results as it meets the speed-bump at around 30 s where it experiences a magnitude of 0.5 g

in y-direction and 0.12g in z-direction. It is worth noting that the IMU is configured to handle up to ± 8 g.

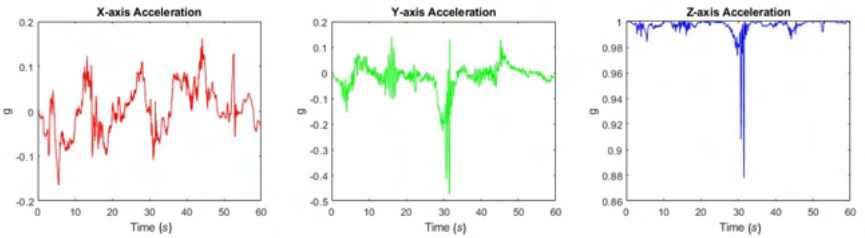

Figure 5.21 Car ride acceleration vibration measurements during 60 s. Impact of road-bump is clearly seen at approximately second 30.

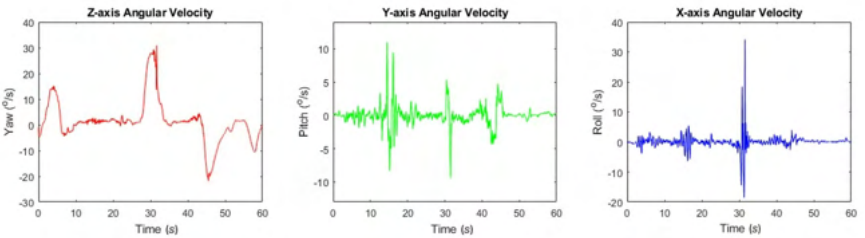

Figure 5.22 Car ride gyroscope vibration measurements in during 60 s. Impact of road-bump is clearly seen at approximately second 30.

The speed-bump effect is even more prominent in the short route gyroscope measurements in *Figure* 5.22 where the x-axis angular velocity or roll experiences as much as 35 dps. Z-axis angular velocity is also affected with around 35 dps, which is somewhat unexpected since the speed-pump is expected to give most of its result in x-axis velocity. However, it could again be because of mechanical motor belt backlash.

Continuing with the long route measurements, the accelerometer magnitude in *Figure* 5.23 are showing similar results as in the short route, with the y-axis showing the largest magnitudes during the 10 minute ride. X and y-axis are expected to show similar result but may differ in magnitude depending on how the camera is oriented in the back of the trunk. The z-axis vibrations are smaller than the other two axes, which is unexpected since the vibrations should be in the vertical direction caused by irregularities in the road surface.

Furthermore, the long route gyroscope measurements in *Figure* 5.24 gives a better intuition of the cameras movement. The impact of the roundabouts is clearly seen at, for example, 90 s and 110 s. Additionally, the impact of a bumpy dirt road is seen

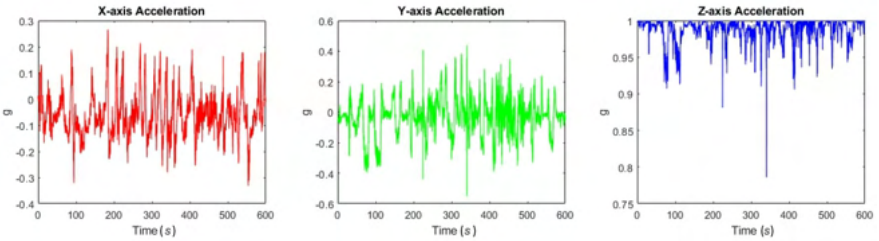

Figure 5.23 Car ride acceleration vibration measurements during 10 minutes.

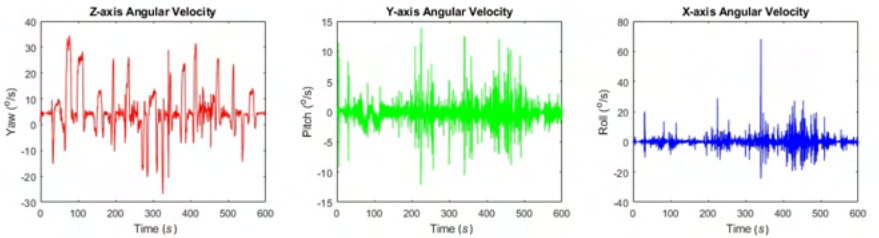

Figure 5.24 Car ride gyroscope vibration measurements during 10 minutes.

between 400 s and 500 s. The maximum vertical x-axis bump is also clearly seen at 350 s with a value of almost 70 dps which overlaps with the minimum measured tampering value in *Figure* 5.15. This means it would not be possible to determine the difference between a bump or vibration and a tampering attempt by only looking at a single 6-axis IMU.

5.5 Conclusion

In *Section* 5.1 we showed that the gyroscope achieved very accurate performance when it was fixed against the tilt axis. An average error of 0.27° was achieved using the Runge-Kutta quaternion integration compared with an average error of 7.0° using regular numerical integration. In conclusion, quaternions are more robust against integration errors than numerical integration, which helps in reducing the drift over time. Quaternions also have the advantage that they avoid potential gimbal lock if they were to be used in a three dimensional scenario and therefore do not lose any DOF.

Furthermore, it was demonstrated that the accelerometer has the smallest calibration error profile at tilt $\pm 90°$ and the largest at tilting 0°. However, the gyroscope achieved satisfying results, indicating that it is helpful to use both in a SFA to obtain better results.

The two different filters, Mahony and Madgwick, were compared in two scenarios: continuous and sweep measurements. Both filters demonstrated the difficulties in keeping an accurate heading estimation over time without any additional reference, especially as the tilt angle passed 0° and further down. The tilt angle successfully kept an accurate tilt estimation, indicating that the SFA does a satisfactory job infusing the two sources using both filters.

The sweep results showed significantly better performance than the continuous results, with a maximum error under 4° for both filters. It is an indication that the 6-axis IMU (gyroscope and accelerometer) is most useful in measuring angle differences rather than absolute position over time, as it is close to impossible to achieve desirable continuous measurements without noticeable drift. However, this does not pose a problem in achieving the purpose of this thesis since the aim is to use it for tampering compensation and not continuous absolute attitude and heading estimation. Therefore, a solution could be to focus on achieving as accurate relative angle difference measurement as possible in combination with a tampering detection mechanism. It is possible to detect tampering, measure the tampered angle, and compensate for the angle difference.

It should be noted that the camera was only rotated in one direction when conducting the continuous measurements. When performing the sweep tests, the camera rotated the direction which had the shortest path from the current starting point. However, it is not expected to result in any difference which direction the camera takes. Still, note that this does not affect the results significantly but should still be mentioned.

In addition, the error interpolation polynomial could be applied to reduce the systematic errors in pan and tilt to receive even more accurate sweep results along the full tilt range. Even though Mahony and Madgwick show similar results overall, Madgwick demonstrates a more systematic error that would be easier to minimize than Mahony.

Additionally, the impact of tampering attempts was measured and compared with regular movements in both pan and tilt. Lastly, the impact of vibrations during a 10 minute and 1 minute car ride was measured. It showed that the tampering and vibration measurements overlapped both in pan and tilt, which means that it would not be possible to determine the difference without any additional measures. One possible solution would be to train a Machine Learning model to recognize the difference between tampering and vibration. However, this approach would be costly in terms of complexity and computation load. A second solution would be to add an IMU and attach it to a fixed, non-moving part of the camera and measure the difference between the fixed and the moving part to determine the difference between "normal" movements and tampering. In such a system, a movement would be classified as a “normal” movement caused by moving objects or vibrations if the two IMUs measure the same values. On the contrary, it would be classified as a

tampering attempt if the IMUs would measure different values.

6

Final System

The final system is the product of testing and comparing through *Chapter* 4 and 5, where some methods were abandoned in favor of others that showed better performance for this particular application. It is important to stress that the main goal is not to achieve a general attitude and heading estimation system but a way to detect and compensate for deviations in movements. At the same time, it needs to be a general solution that proves to be robust in any environment. The cases that are presented in *Section* 1.2 and handled in this thesis are repeated:

1. When the camera is mounted on a non-moving object:
    a) Camera is tampered while not moving.
    b) Camera is tampered while moving.
2. Tampering when camera is moving.
    a) Camera is tampered while not moving.
    b) Camera is tampered while moving.

The following chapter will demonstrate a system that fulfills all of the above cases.

Section 6.1 starts by presenting the design of the final system, in terms of an explanation of its hardware and software features in addition to the implementation and the used parameters. Thereafter, *Section* 6.3 presents the economic aspects of the system in relation to the previous mentioned solutions. The results are then presented in *Section* . The last vibration tolerance results are lastly presented in *Section* 6.4.3.

6.1 Design

The final system uses a modification of the general Madgwick orientation filter, which we call the *Motion Triggered Differential Madgwick* (MTDM) that makes use of a 6-axis IMU in order to track relative angular movements between two idle positions reliably. It follows the *No Motion No Integration* (NMNI) principle, which means that it will only continue quaternion integration using an SFA as long as it has trespassed the *Motion Threshold*. It will continue until it has reached the *No-Motion Threshold* and keep its previous position in quaternion space. We decided on using the Madgwick filter, which proved to have desirable performance in *Chapter* 5. In principle, this method could be used to measure absolute position as well. However, the error would still be accumulated for each motion, making it an unreliable method over time. Focusing on the relative angle differences makes it possible to achieve high resolution over time, even though the absolute position in quaternion space has drifted due to integration and other errors.

6.1.1 Motion Triggered Differential Madgwick

The basic principle of the MTDM scheme is shown in *Figure* 6.1 where the red parts of the curve highlight the intervals where the quaternion integration is activated, whereas the black parts show the intervals where it is idle. Using the results from the tampering and vibration results in *Section* 5, the angular measurements from the gyroscope proved to be the most reliable source for movement detection since tampering is dominantly angular rather than linear and vibrations dominantly linear rather than angular, which means that it is not only detected tampering best but also picks up noise less than the accelerometer. The gyroscope measurements go through a low-pass filter before it checks whether the "motion threshold" has trespassed. If it a motion would occur as in *Figure* 6.1 the Madgwick filter is activated, propagating the quaternion state $\dot{q}_{est,1}$ until it reaches the "no-motion threshold" and the next idle quaternion state $\dot{q}_{est,2}$ and $\dot{q}_{est,3}$ after the next movement. At each idle quaternion state, the quaternion state space is converted to Tait-Bryan angles using *Equation* 2.15, from which the difference between the latest two consecutive angles is calculated.

The state changes can also be expressed in terms of "is moving" and "was moving". If the state change is "is not moving" $\longrightarrow$ "was not moving", nothing will happen. If the change is from "is moving" $\longrightarrow$ "was moving" it will continue the Madgwick integration until it reaches the state change "is not moving" $\longrightarrow$ "was moving" from which the angle difference, $\boldsymbol{\Delta}_{\boldsymbol{mov}}$, between the current state, j and previous state, $j-1$, is calculated as

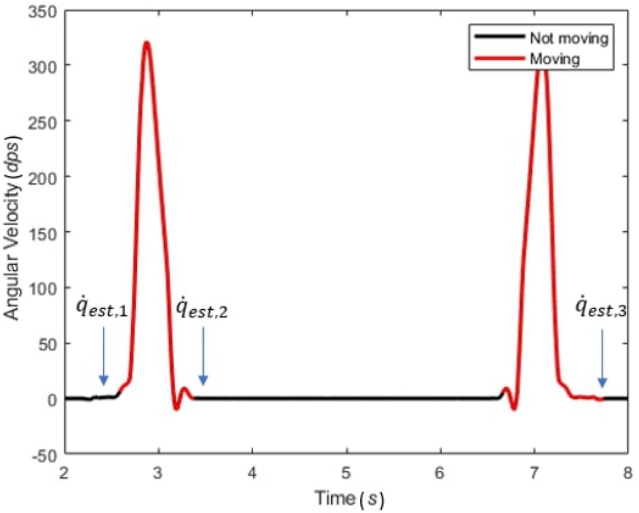

Figure 6.1 Demonstrates the basic principle of the MTDM algorithm, where the quaternion integration is running during the red part of the curve as it reaches the motion threshold and then paused at a new state as it reaches back to the no-motion threshold.

$$\boldsymbol{\Delta_{mov}} = \begin{bmatrix} \Delta\varphi_{j,mov} \\ \Delta\theta_{j,mov} \\ \Delta\psi_{j,mov} \end{bmatrix} = \begin{bmatrix} \varphi_{j,mov} - \varphi_{j-1,mov} \\ \theta_{j,mov} - \theta_{j-1,mov} \\ \psi_{j,mov} - \psi_{j-1,mov} \end{bmatrix} \tag{6.1}$$

This system is enough to achieve the first goal of the thesis, to be able to detect and correct when tampering has occurred when the camera is mounted on a non-moving object presented in *Section* 1.2. Since the step-motor state is known in software, we know when it is moving and when it is not, meaning that it is possible to determine both *(a)* and *(b)*. If the camera has been tampered with when the step-motor is not active, the difference from the latest known idle state is calculated using the MTDM after which the step-motor can be corrected. If the camera has been tampered with when the step-motor is active, the measured angle from the MTDM algorithm is compared with the expected angle and thereafter corrected.

6.1.2 Double IMU sensors

Only using the MTDM alone is not enough to achieve the second goal of the thesis since the camera angle information would be lost if the whole camera was moving. An example would be if the camera pan motor moves 50° and the whole camera also moves 50°, it would compensate for 100° since it would be the total expe-

Figure 6.2 Axis Q6215 camera showing the possible placements of the moving and fixed IMU.

rienced rotation for the IMU. In order to also allow the camera to be mounted on moving objects, a second IMU is placed in the fixed part of the camera so that it does not rotate along with the pan and tilt motors, as shown in *Figure* 6.2. The second IMU also runs the MTDM algorithm but is triggered by the moving IMU threshold instead of its own. Once the moving IMU has met the lower threshold, the angular difference of the moving IMU is calculated as in *Figure* 6.1 as well as the angular difference of the fixed IMU, $\boldsymbol{\Delta_{fix}}$, between the current state, j and previous state, $j-1$, calculated as

$$\boldsymbol{\Delta_{fix}} = \begin{bmatrix} \Delta\varphi_{j,fix} \\ \Delta\theta_{j,fix} \\ \Delta\psi_{j,fix} \end{bmatrix} = \begin{bmatrix} \varphi_{j,fix} - \varphi_{j-1,fix} \\ \theta_{j,fix} - \theta_{j-1,fix} \\ \psi_{j,fix} - \psi_{j-1,fix} \end{bmatrix}. \tag{6.2}$$

The total angular difference between the moving angular difference and the fixed angular difference, $\boldsymbol{\Delta_{tot}}$, at a state, j, is then simply subtracted:

$$\boldsymbol{\Delta_{tot}} = \boldsymbol{\Delta_{mov}} - \boldsymbol{\Delta_{fix}}. \tag{6.3}$$

This way, the second goal of the thesis, to be able to detect and correct potential tampering on a moving camera, would be fulfilled in both case *a)* and *b)*.

6.1.3 Motion State Sampling

As we found out in *Chapter* 5.2.1, the SFA algorithm suffers from the drift that increases with time, which poses a problem to the proposed system as the motions

events become longer. A camera mounted on a car that would go in and out of roundabouts would perhaps not meet the No-Motion threshold for some time. Additionally, the drift of the two IMU:s would perhaps not drift at the same speed or direction, which would produce inaccurate difference calculations. Therefore, an additional *Motion State Sampling* (MSS) mechanism is introduced to compensate for this drift. The basic principle of the MSS is that it samples the quaternion space at a frequency f_{mss} during the time that both the fixed and the moving IMU is moving. It is demonstrated in *Figure* 6.3, where $\bar{q}_{est,j}$ represents the regular quaternion states and the $\bar{q}_{mss,j}$ represents the extra quaternion states triggered by the MSS mechanism at a frequency of 0,1 Hz. With this mechanism in place, if the fixed IMU mounted on a car would experience angular movements between t=260 to t=340 it would detect and correct for the potentially tampered difference between the fixed and the moving IMU at each MSS sample, the same way it was calculated in *Equation* 6.3.

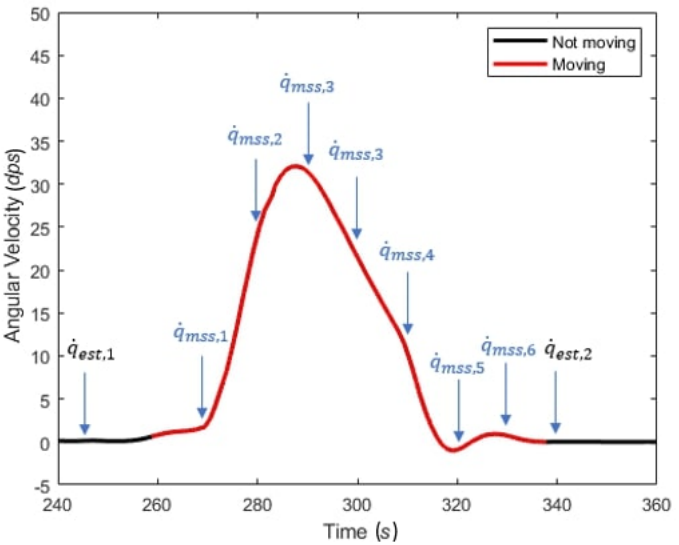

Figure 6.3 Principle of the MSS function, where the red interval demonstrates where it is in moving state, and black interval the non-moving state.

6.1.4 Interpolation Error Compensation

As discussed in *Chapter* 5.2.3, the sweep measurements in *Chapter* 5.2.2 were also a way to calibrate against systematic errors of the IMU. Each new product could perform this factory calibration with the step-motor movements as a reference to map out the error profile to further increase the accuracy. Testing showed that a 2D interpolation surface $f_{tilterror}(\psi, \varphi)$ of order ψ^2 and φ^3 was appropriate for tilt and

a surface $f_{panerror}(\psi, \varphi)$ of order ψ^3 and φ^2 for pan. The polynomials used in this particular system can be seen in *Appendix* 8.1.

6.2 Sensor Calibration

As mentioned throughout the report, it is important to include measures to reduce drift. Therefore, the gyroscope is initially calibrated by averaging the first 500 samples in a non-vibrating environment, which are saved and subtracted from future samples to reduce angular off-sets. Additionally, since the accelerometer measures angle in the inertial frame, it is necessary to rotate the measurement to a fixed reference frame. The reference frame is the same as the calibration frame, which has a preset orientation in the camera. Since the camera does not have any reliable way to measure absolute position in pan, it is necessary to have a "homing sensor" that guides the camera to its calibration state. The calibration orientation tilt angle is found by observing the absolute tilt difference between the moving and the fixed IMU to find a preset calibration position in tilt relative to the direction of gravity. It is achieved, by sampling the first 500 accelerometer values from which roll and pitch values are calculated using the Direct Tait-Bryan Angle method for each IMU. These reference values are then used to construct a rotation matrix used to rotate future accelerometer readings to get them in the reference frame.

6.2.1 Software Design

The software implementation of the algorithm is described in the flowchart in *Figure* 6.4. The total *Lines Of Code* (LOC) including embedded drivers ended at 2550.

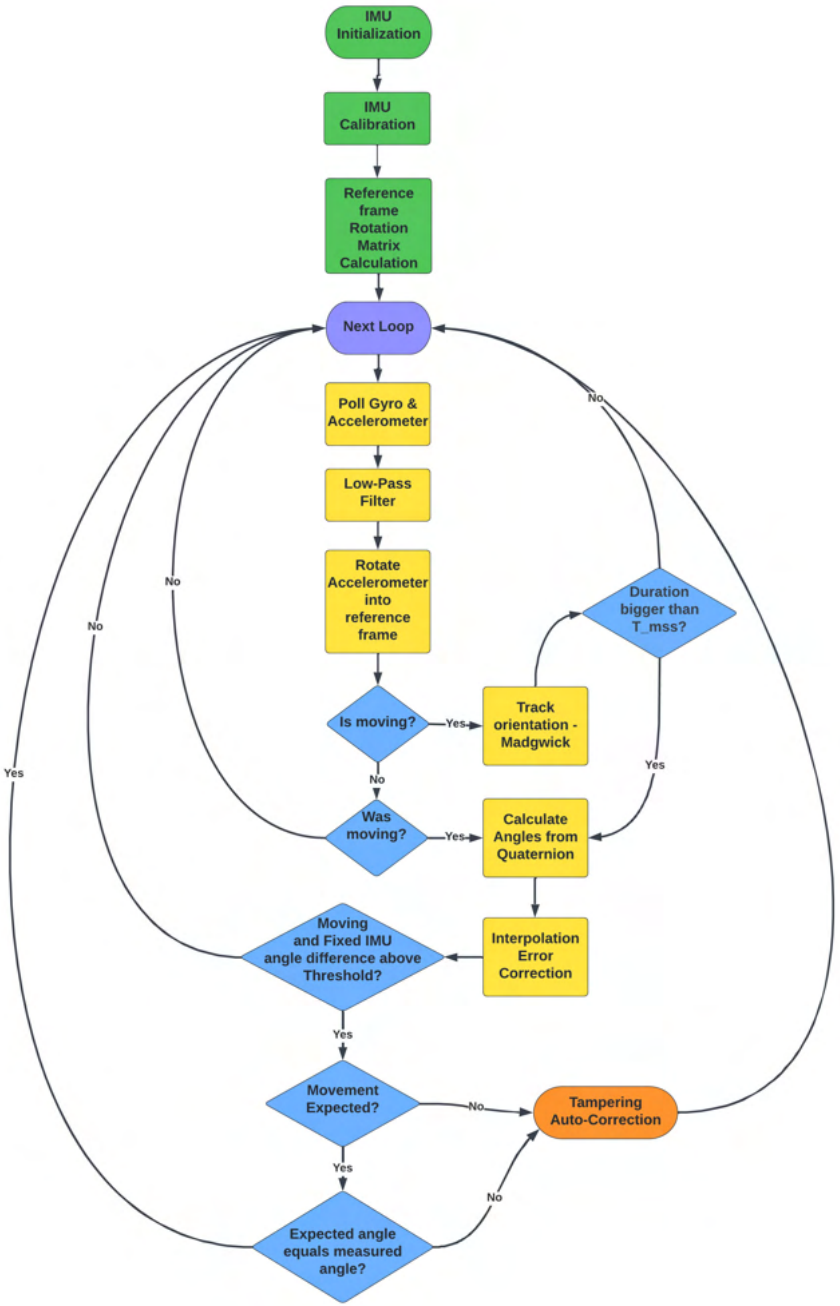

Figure 6.4 Software design flowchart of the final system.

6.2.2 Parameters

- **Sensor Resolution**: The accelerometer resolution was determined to ± 8 g in order to get as accurate measurements as possible while still being within the range of vibrations. The gyroscope resolution was set to ± 100 dps in order to be able to read the fastest motor movements of 700 dps.
- **ICM20602 Hardware Low-pass Filter**: A cut-off frequency of $\omega_{cut-off}$ = 5.7 Hz was applied to the raw accelerometer data and a cut-off frequency of $\omega_{cut-off}$ = 11.6 Hz was applied to the raw gyroscope data.
- **Software Exponential Moving Average**: The weighting factor in the EMA low-pass filter was set to α = 0.2 for both the accelerometer and gyroscope data.
- **Sampling time**: The IMU measurements was polled at a rate of T_s =20 ms per poll - corresponding to a frequency of 50 Hz.
- **Madgwick Filter constant**: The Madgwick filter constant was set to β =0.1 after experimental testing of optimal value.
- **Motion threshold**: The motion threshold was set to $\omega_m = 5$ dps after analysis of the results in *Section* 5.3 and 5.4.
- **No-Motion threshold** : The no-motion threshold was set to ω_{nm} =0.2 dps after analysis of the results in *Section* 5.3 and 5.4
- **Motion State Sampling time**: A reasonable MSS sampling time was set to T_{MSS} =10 s.
- **Total Difference Tampering Threshold:** The total difference tampering threshold was set to Δ_{tot} = 3 $^\circ$ since tampering showed to be extremely difficult below this value.

6.3 Economy

The only hardware needed, and only expense, for this implementation is two IMUs. In this final design, the ICM20602 mentioned in *Section* 3.2 is used. The cost of one unit can be seen in *Table* 3.3. As mentioned, two IMUs are needed and the price for them can be seen in *Table* 6.1. The total costs for the existing feedback solutions are repeated and put into relation to the new IMU feedback solution cost in *Table* 6.2. However, this comparison is not completely fair. The magnetic- and optical solution costs are prices negotiated between Axis and the reseller. It is possible to reduce prices when the volumes are big. At this time, the cost for the IMU feedback solution is calculated with prices found at a reseller. If this solution would

be integrated into a product then the volumes of IMUs would be big and the prices are negotiable. A reduced cost of IMUs would lead to less than a total of $4.80.

Table 6.1 Hardware cost for new feedback solution

Unit price ICM20602:	$2.40
Total cost:	$4.80

Table 6.2 The total cost for the different feedback solutions and their relation to the IMU feedback cost.

	IMU	Magnetic	Optical
Total cost:	$4.80	$27.41	$10.88
In relation to IMU cost:	100%	571%	227%

6.4 Performance results

6.4.1 Mounted on non-moving object

The resulting precision (error in degrees) benchmarked against the magnetic encoder, when mounted on a non-moving object is compiled in *Table* 6.3. The tilt and pan error angle was measured 50 times with a non-moving camera head and 50 times with a moving camera head, both in a quiet office environment.

Table 6.3 Results of final system mounted on a non-moving object with 50 samples for moving camera head and 50 samples for non-moving camera head.

	Non-moving Camera		**Moving Camera**	
	Pan	***Tilt***	***Pan***	***Tilt***
Max	2,98	2,09	2,18	1,79
Min	0,03	0,04	0,06	0,03
Mean	1,24	0,93	0,76	0,50
Median	1,18	0,99	0,66	0,37
RMSE	1,46	1,11	0,92	0,69
Std. dev	0,78	0,62	0,53	0,48

6.4.2 Mounted on moving object

The error against the magnetic encoder's estimation, when mounted on a moving object is compiled in *Table* 6.4. The test was performed with the camera mounted inside the trunk of a car while driving in both city and country environments. Because of the difficulty of testing in a moving environment, 15 samples were taken both for the case of non-moving camera tampering and moving camera tampering, compared with the fixed mounted tests that were easier to perform.

Table 6.4 Results of final system mounted on a moving object with 15 samples for moving camera head and 15 samples for non-moving camera head.

	Non-moving Camera		**Moving Camera**	
	Pan	***Tilt***	***Pan***	***Tilt***
Max	1,49	4,22	1,0	4,38
Min	0,26	1,34	0,06	0,81
Mean	0,76	3,06	0,59	2,63
Median	0,42	3,19	0,66	2,87
RMSE	0,82	3,24	0,68	2,93
Std. dev	0,58	1,16	0,37	1,4

6.4.3 Vibration Tolerance

As a tolerance test on the final system design, the IMU was put on a vibrator board that was set to vibrate with different magnitudes of gravity and frequencies. The setup on the vibrator board can be seen in *Figure* 6.6. The test was done to simulate possible vibrations that the camera can be exposed to when mounted in a customer's environment. The IMU was mounted a bit differently from the other setups to ensure it would not affect the vibrations more than the camera itself. Holes were drilled in the camera, and then the IMU was screwed into it and then glued to make it more robust. For example *Figure* 3.4 shows that the IMU was only taped to the camera's chassi before; this worked fine for the tests that were relevant at that time. The new setup can be seen in *Figure* 6.5. This setup was not applied initially to make the setups the same and avoid tape because this test was not planned. Because of the limited time for this master thesis, it was not certain there would be time to do this test.

In total, three different tests were made. The goal of two of the tests was to find a threshold for magnitudes of gravity that the system identified as tampering, both for continuous vibrations and shock. Those magnitudes can be seen in *Table* 6.5.

Figure 6.5 IMU mounted on moving part of camera for vibration tolerance test.

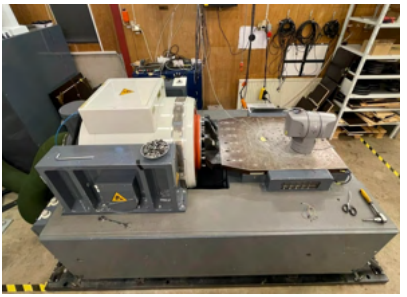

Figure 6.6 The setup with vibrator and camera mounted on the table.

In the continuous vibration mode, a resonance frequency for the whole camera was found at approximately 17 Hz and was used when finding the tolerance. The newly designed feedback system could handle much higher shock accelerations than continuous vibrations. A reason for this could be because the resonance frequency was used. If another frequency was used without amplification, the system might have been able to handle greater accelerations. However, since vibrations at resonance frequency are a worst-case scenario, it was more urgent to find this limitation. It was important to test both modes because of the customers varying environments exposed the products to. Shock is good to test if the camera is placed in, e.g., a city with easy access for someone to kick at the camera. Continuous vibrations could be good to test if a customer, e.g., places the camera on a crane.

Table 6.5 Tolerance at the different vibration modes tested.

	Max magnitude before tampering alert	Resonance frequency
Continuous vibrations	0.75 g–1 g	17 Hz
Shock	12.5g–15g	-

The last of the three tests was to test tampering during continuous vibration mode at resonance frequency with a magnitude of 0,1 g, see *Table* 6.6. The errors are seen in the same table result from an average of ten tampering attempts. As with previous tampering attempts, the IMU's estimation of tampering was compared to the difference in the magnetic encoders' estimation of position. Due to worn mechanics from all previous tampering there is backlash, which resulted in unwanted movements in the camera during the vibrations. Those movements made the magnetic encoder

uncertain in the decimals in the position estimation, making the reading unreliable. However, the error was satisfyingly low for that many vibrations.

Table 6.6 Errors from ten tampering attempts at the presented settings.

Mode	Frequency	Magnitude	Pan error	Tilt error
Continuous vibration	17 Hz	0.1 g	$\pm 1.06°$	$\pm 0.68°$

7

Discussion

7.1 Solutions for Tampering Detection Comparison

The resulting system was proven to be a viable alternative to step-motor feedback for tampering detection alongside with the current solutions at Axis: the magnetic encoder and the optical encoder. Comparing the three, it is clear that the magnetic encoder has superior performance, with an average accuracy of $\pm 0.005^{\circ}$, but with a hefty price tag of $27.41 in bulk. In the time of writing, there is a global semiconductor shortage affecting almost all electronics companies globally, and the fact that there are currently only two different manufacturers of magnetic encoders that fit the Q6215 could eventually be a disadvantage. In times of supply shortage, it could therefore become a problem with to specific solutions which is difficult to find second sources of. Even if the proposed IMU solution, achieving an average precision around $\pm 1^{\circ}$, is less accurate than the magnetic encoder, it is still an advantage that there are many more 6-axis IMU manufacturers on the market from this perspective. A second advantage of the proposed IMU solution is the price-point of $4.80, almost 6 times cheaper than the magnetic encoder and 2 times cheaper than the optical.

Depending on the product requirements, the accuracy of the proposed IMU solution could still be too low, for some applications. In some of the PTZ cameras that offer up to 30x zoom, 1° error could potentially shift the whole image, in which the tampering auto-correction would not too much help in that particular situations. However, in some other products in Axis product segments without zoom, there is the optical encoder that provides on average $\pm 9^{\circ}$. In these cameras, the IMU solution would be a very viable alternative to the optical encoder. Additionally, even if the optical encoder is not as expensive as the magnetic encoder, the proposed IMU solution still has an advantage in terms of cost.

An additional advantage of the IMU is that is very easy to integrate into existing products. For example, the Q6215 already has one IMU on the power PCB that resides in the fixed part of the camera, which means that only one additional IMU

would have to be put on one of the existing cards in the moving parts. The mechanical footprint of this solution is therefore minimal comparing with the magnetic and the optical encoder solution.

7.2 Limitations of Final System

The biggest difference between the encoder solutions and the proposed IMU solution is that the encoder solutions measure absolute orientation, whereas the IMU solutions measure angular movements. It means that the IMU cannot be used in order to determine the absolute position, which is useful when we want the camera to move to a preset position, for example a "homing" position that it goes to after reboot, or a "calibration" position that it uses during calibration. If we want this properties in the IMU solution, an additional homing sensor would be needed, as already pointed out in *Section* 6.2. A solution that is used in some of today's product is to have a magnet that is read by a magnetic hall sensor, which solves this problem easily, but the number of possible preset positions is then constrained by the number of magnet flags in the camera.

A second solution would be to incorporate the magnetometer, which was analyzed in *Section* 4.3, in order to add this functionality. Then no additional magnetic flag would be needed within the camera, since it would be possible for the magnetometer to measure the absolute orientation of the moving IMU relative to the fixed. In addition, it would add the functionality to move along the magnetic poles of earth, a feature that could be valuable in maritime applications. However, the magnetometer was dropped in the final system due to its sensitivity towards magnetic disturbances which could pose a big problem to its functionality as it is integrated near the stepmotors. Additionally, the magnetometer required careful calibration and was too sensitive to be used as a reference in the final angle difference calculations, since the system is required to show robust performance in all environments.

Currently the designed feedback system can not handle changes in pitch and roll in the fixed part of the camera (when the whole camera is pitching and rolling) if the two IMUs coordinate systems are not aligned. This is due to the lack of a reference in the horizontal plane, i.e., for the x- and y-axes. There is a need for a magnetometer or similar to fix the axes at a certain direction, then the pitch and roll angles can be compared in a correct way. For the z-axis there is no problem since the tilt of the IMUs can be computed with help from gravity and then corrected. The challenge to find a reliable reference can be tough. A magnetometer can be disturbed from the environment and hence show incorrect data which could lead to a faulty rotation matrix. This will be the case if the IMUs magnetometers are not affected by the exact same disturbances.

7.3 Further work

As mentioned in *Section* 7.2, there is a need for an additional reference to fix two of the three axes in the IMU for a more reliable result. Because as of now, the system can not handle permanent changes in pitch and roll since there might be a misalignment between the IMUs coordinate systems that can not be transformed, and to get a general feedback solution a transformation is needed. In this thesis it has been investigated to use IMUs with magnetometers, but since these sensors are reliable on the environment, this is not a good option. Instead other solutions have to be investigated. For example, it would be a good idea to test using permanent magnets and a Hall sensor. If the magnets are aligned for both IMUs then axes could be fixed and the IMUs could be transformed to the same coordinate system.

Since this is a master thesis we have not had the resources to access the signals from the stepper motors. Something to investigate could be to involve these signals in the control loop in combination with a homing sensor. The homing sensor could consist of, e.g, a Hall sensor and magnets. Then the feedback is not reliable on the environment, and if both IMUs have the same alignment for sensor and magnets, they share homing position. This could potentially increase robustness of the system. If knowing the motors position with respect to the homing sensor, and tracking how much tampering occured, then it is easy for the system to find home and then go back to the position before tampering, potentially with smaller error than our final system.

It could also be interesting to test using one IMU for pan, one IMU for tilt and one IMU in a non-moving part, instead of using one IMU on the moving part where the gyro and accelerometer are used for pan and accelerometer used for tilt. *Figure* 5.3 shows how the gyro outperforms the accelerometer for almost all angles between $\pm 90^\circ$ when the IMU is placed so that its yaw angle is the cameras tilt angle. A test to put the current solution, with two IMUs, in relation to using three IMUs could be useful to compare performance. The cost would in total, if using three IMUs, be less than any of the already existing feedback solutions.

Tests that there was not time for but could still be good are temperature and a long-time accuracy test. Since Axis cameras can be found all over the world and should be able to handle temperatures from -20° to 50° then it is crucial for the tampering feedback to do so as well. The long-term test would be good to see if the accuracy of the feedback gets worse with time.

The new feedback system could also be integrated with another use-case. Since having a gyroscope, the camera could be instructed to stay with the same footage if, e.g., mounted on a moving object like a crane.

8

Conclusion

When wrapping up this master thesis and looking back at the results for this proof-of-concept we can see some satisfying results. From start it was stated that the solution should only be compared to the magnetic feedback because of its superiority in resolution compared to the optical feedback. The goal was to achieve as close estimations as possible and hence, minimize the error between IMU output and magnetic encoder output. Inherited weaknesses of the IMU, such as drift, noise and interference sensitivity made it difficult to achieve an accurate solution. Therefore the original idea with absolute position estimation was redirected to estimate relative movements.

Advanced signal processing and sensor fusion algorithms were used to get a system that could handle the demands put on it by the environment. An accuracy of $\pm 1.0^{\circ}$ in pan and $\pm 0.7^{\circ}$ in tilt, compared to the magnetic feedback, was achieved when the camera was mounted on a fixed object. As the camera was mounted on a moving object, the accuracy in tilt was decreased but still more than three times as accurate as the optical encoder. The proposed system using IMUs also helps in reducing mechanical complexity and reducing cost, compared to existing solutions. Additionally, the system proved to handle tough vibrations up to 1 g and shock tests up to 15g, which are accelerations over the specification requirements of the tested camera model.

Further work is however needed in order to integrate the new feedback system into cameras, though this proof-of-concept has shown that using IMUs for feedback on a PTZ camera can be a great cost reduced option to the optical feedback. However, the new designed concept might have a hard time competing with the magnetic feedback because of its very good resolution and independence on the environment. It can be concluded that keeping the magnetic encoders for the more premium PTZ cameras that have zoom is better, since a single degree error can change a zoomed footage completely.

Bibliography

Allgeuer, P. and S. Behnke (2018). "Fused angles and the deficiencies of euler angles". In: DOI: 10.1109/IROS.2018.8593384.

Cirillo, P., A. Cirillo, G. De Maria, C. Natale, and S. Pirozzi (2016). "A comparison of multisensor attitude estimation algorithms". In: pp. 529–539. ISBN: 9781498745710.

Fan, B., Q. Li, and T. Liu (2017). "How magnetic disturbance influences the attitude and heading in magnetic and inertial sensor-based orientation estimation". eng. *Sensors (Basel, Switzerland)* **18**:1. s18010076[PII], p. 76. ISSN: 1424-8220. DOI: 10.3390/s18010076. URL: https://doi.org/10.3390/s18010076.

Freidovich, L. B. (2017). "Control methods for robotic applications". In: pp. 23–45.

InvenSense, T. (2021). "Icm-20948 datasheet". URL: https://invensense.tdk.com/download-pdf/icm-20948-datasheet/.

Jones, D. W. (2001). *Control of Stepping Motors - A Tutorial*. Yeadon and A. W. Yeadon, McGraw-Hill.

Kok, M., J. D. Hol, and T. B. Schön (2017). *Using Inertial Sensors for Position and Orientation Estimation*.

Kuipers, J. (2020). *Quaternions and Rotation Sequences: A Primer with Applications to Orbits, Aerospace and Virtual Reality*. Princeton University Press. ISBN: 9780691211701. URL: https://books.google.se/books?id=p%5C_3RDwAAQBAJ.

Ludwig, S. A. and K. D. Burnham (2018). "Comparison of euler estimate using extended kalman filter, madgwick and mahony on quadcopter flight data". In: *2018 International Conference on Unmanned Aircraft Systems (ICUAS)*, pp. 1236–1241. DOI: 10.1109/ICUAS.2018.8453465.

Madgwick, S. O. H., A. J. L. Harrison, and R. Vaidyanathan (2011). "Estimation of imu and marg orientation using a gradient descent algorithm". In: *2011 IEEE International Conference on Rehabilitation Robotics*, pp. 1–7. DOI: 10.1109/ICORR.2011.5975346.

Mahmood, D., N. Javaid, M. Imran, U. Qasim, and Z. Khan (2016). "Chapter 8 - data fusion for orientation sensing in wireless body area sensor networks using smart phones". In: Dobre, C. et al. (Eds.). *Pervasive Computing*. Intelligent Data-Centric Systems. Academic Press, Boston, pp. 231–252. ISBN: 978-0-12-803663-1. DOI: https://doi.org/10.1016/B978-0-12-803663-1.00008-5. URL: https://www.sciencedirect.com/science/article/pii/B9780128036631000085.

Mansur, V., S. Reddy, S. R, and R. Sujatha (2020). "Deploying complementary filter to avert gimbal lock in drones using quaternion angles". In: *2020 IEEE International Conference on Computing, Power and Communication Technologies (GUCON)*, pp. 751–756. DOI: 10.1109/GUCON48875.2020.9231126.

MATLAB (n.d.). *Curve fitting toolbox*. URL: https://se.mathworks.com/products/curvefitting.html.

Pedley, M. (2013). "Tilt sensing using a three-axis accelerometer". *NXP Freescale Semiconductor- Application Note 1*, pp. 2012–2013. URL: https://www.nxp.com/files-static/sensors/doc/app_note/AN3461.pdf.

Pedley, M. (2015). "High-precision calibration of a three-axis accelerometer". *NXP Freescale Semiconductor- Application Note*. URL: https://www.nxp.com/docs/en/application-note/AN4399.pdf.

Sawicki, A., Z. Slanina, and A. Linkel (2017). "Compensation of hard- and soft-iron distortions is magnetometer measurement data". In: Romaniuk, R. S. et al. (Eds.). *Photonics Applications in Astronomy, Communications, Industry, and High Energy Physics Experiments 2017*. Vol. 10445. International Society for Optics and Photonics. SPIE, pp. 1715–1723. DOI: 10.1117/12.2280794. URL: https://doi.org/10.1117/12.2280794.

Schweber, B. (2021). *Options abound when selecting a sensor for motor feedback*. Accessed: 2022-01-24. URL: https://www.mouser.se/applications/selecting-sensors-for-motor-feedback/.

Seybold, J., A. Bülau, K.-P. Fritz, A. Frank, C. Scherjon, J. Burghartz, and A. Zimmermann (2019). "Miniaturized optical encoder with micro structured encoder disc". *Applied Sciences* **9**:3. ISSN: 2076-3417. DOI: 10.3390/app9030452. URL: https://www.mdpi.com/2076-3417/9/3/452.

Wittenmark, B., K. J. Åström, and K.-E. Årzén (2002). *Computer Control: An Overview*. IFAC Professional Brief.

Wu, J. (2019). "Real-time magnetometer disturbance estimation via online nonlinear programming". *IEEE Sensors Journal* **19**:12, pp. 4405–4411. DOI: 10.1109/JSEN.2019.2901925.

Yang, W., A. Bajenov, and Y. Shen (2017). "Improving low-cost inertial-measurement-unit (imu)-based motion tracking accuracy for a biomorphic hyper-redundant snake robot". *Robotics and Biomimetics* **4**:3. ISSN: 2197-3768.

DOI: 10.1186/s40638-017-0069-z. URL: https://doi.org/10.1186/s40638-017-0069-z.

Yi, C., J. Ma, H. Guo, J. Han, H. Gao, F. Jiang, and C. Yang (2018). "Estimating three-dimensional body orientation based on an improved complementary filter for human motion tracking". eng. *Sensors (Basel, Switzerland)* **18**:11. s18113765[PII], p. 3765. ISSN: 1424-8220. DOI: 10.3390/s18113765. URL: https://doi.org/10.3390/s18113765.

Appendix

8.1 Error Interpolation Polynomial

$$f_{tilterror}(\psi,\varphi) = p_{00} + p_{10}\psi + p_{01}\varphi + p_{20}\psi^2 + p_{11}\psi\varphi + p_{02}\varphi^2 + p_{21} * \psi^2\varphi + p_{12}\psi\varphi^2 + p_{03}\varphi^3 \tag{8.1}$$

Tilt error coefficients with 95% confidence bounds:

- p_00 = 0.8559 (0.4538, 1.258)
- p_10 = 1.768e-06 (-0.003616, 0.003619)
- p_01 = 0.04034 (0.02978, 0.05089)
- p_20 = 3.295e-05 (9.978e-06, 5.593e-05)
- p_11 = 3.532e-06 (-3.422e-05, 4.128e-05)
- p_02 = -0.0001032 (-0.0001677, -3.871e-05)
- p_21 = 2.714e-07 (-8.596e-08, 6.287e-07)
- p_12 = 7.007e-08 (-5.805e-07, 7.206e-07)
- p_03 = -4.74e-06 (-6.105e-06, -3.376e-06)

$$f_{panerror}(\psi,\varphi) = p_{00} + p_{10}\psi + p_{01}\varphi + p_{20}\psi^2 + p_{11}\psi\varphi + p_{02}\varphi^2 + p_{30}\psi^3 + p_{21}\psi^2\varphi + p_{12}\psi\varphi^2 \tag{8.2}$$

Pan error coefficients with 95% confidence bounds:

- p_{00} = -1.774 (-1.98, -1.568)
- p_{10} = 0.007119 (0.004029, 0.01021)
- p_{01} = 0.00967 (0.007317, 0.01202)
- p_{20} = -5.38e-06 (-1.961e-05, 8.855e-06)
- p_{11} = -7.878e-06 (-2.678e-05, 1.102e-05)
- p_{02} = 0.0001361 (0.0001038, 0.0001684)
- p_{30} = -1.487e-07 (-2.914e-07, -5.992e-09)
- p_{21} = 6.914e-08 (-1.098e-07, 2.481e-07)
- p_{12} = -3.358e-07 (-6.614e-07, -1.015e-08)

Lund University
Department of Automatic Control
Box 118
SE-221 00 Lund Sweden

Document name
MASTER'S THESIS

Date of issue
May 2022

Document Number
TFRT-6161

Author(s)
Ludvig Hansson
Måns Lindeberg

Supervisor
Marcus Romner, Axis Communications
Anton Cervin, Dept. of Automatic Control, Lund University, Sweden
Kristian Soltesz, Dept. of Automatic Control, Lund University, Sweden (examiner)

Title and subtitle
PTZ Camera Tampering Correction Using IMUs

Abstract

The Pan-Tilt-Zoom (PTZ) camera is a type of camera that covers large areas, up to 360°, in addition to zoom. Some of these cameras are susceptible to tampering, which means that an additional angle measurement feedback is necessary to detect such attempts. This thesis has evaluated the possibility of using MEMS-based IMUs to solve this problem. An advantage of such a system over other solutions, such as optical and magnetic encoders, is the decreased cost and complexity. The difficulty of using IMUs is that they are susceptible to drift in horizontal rotations in pan and require advanced signal processing to be reliable in demanding environments. Results showed that it was possible to correct tampering by using two IMUs, one on the fixed part of the camera and one on the moving part of the camera. It was then possible to track and correct tampering attempts with an average error of 1.0◦ in pan and 0.7◦ in tilt. The solution works when the camera is mounted on both fixed and moving objects. Notably, the solution proved to be much cheaper than alternative methods.

Additionally, it proved to be robust against vibrations and shocks and within the performance requirements of the tested model. Additional methods were suggested for the system to track absolute orientation, for example, to be able to move the camera to pre-set positions. However, further work is needed to increase robustness in applications where the camera is mounted on objects that can rotate in roll or pitch.

Keywords

Classification system and/or index terms (if any)

Supplementary bibliographical information

ISSN and key title
0280-5316

ISBN

Language
English

Number of pages
1-88

Recipient's notes

Security classification

http://www.control.lth.se/publications/